Properties of Daily Helium Fluxes
- SUPPLEMENTAL MATERIAL -

(AMS Collaboration)

For references see the main text.

Detector.—AMS is a general purpose high energy particle physics detector in space. The layout of the detector is shown in Fig. S1. The main elements are the permanent magnet, the silicon tracker, four planes of time of flight (TOF) scintillation counters, the array of anticoincidence counters (ACCs), a transition radiation detector (TRD), a ring imaging Čerenkov detector (RICH), and an electromagnetic calorimeter (ECAL). The three-dimensional imaging capability of the 17 radiation length ECAL allows for an accurate measurement of the energy E and the shower shape of $e^{\pm}$. The AMS coordinate system is concentric with the magnet. The x axis is parallel to the main component of the magnetic field and the z axis points vertically with $z = 0$ at the center of the magnet. The (y-z) plane is the bending plane. Above, below, and downward- going refer to the AMS coordinate system. The central field of the magnet is 1.4 kG. Before flight, the field was measured in 120 000 locations to an accuracy of better than 2 G. On orbit, the magnet temperature varies from -3 to $+20°$C. The field strength is corrected with a measured temperature dependence of $-0.09\%/°$C. The tracker has nine layers, the first ($L1$) at the top of the detector, the second ($L2$) just above the magnet, six ($L3$ to $L8$) within the bore of the magnet, and the last ($L9$) just above the ECAL. $L2$ to $L8$ constitute the inner tracker. Each layer contains double-sided silicon microstrip detectors which independently measure the x and y coordinates. The tracker accurately determines the trajectory of cosmic rays by multiple measurements of the coordinates with a resolution in each layer of 6.5 μm for helium in the bending (y) direction. Together, the tracker and the magnet measure the rigidity R of charged cosmic rays.

Each layer of the tracker provides an independent measurement of charge Z with a resolution of $\sigma_Z/Z = 6.4\%$ for helium. Overall, the inner tracker has a resolution of $\sigma_Z/Z = 3.4\%$ for helium.

As seen from Fig. S1, two of the TOF planes are located above the magnet (upper TOF) and two planes are below the magnet (lower TOF). The overall velocity ($\beta = v/c$) resolution has been measured to be $\sigma(1/\beta) = 0.02$ for helium. This discriminates between upward- and downward-going particles. The pulse heights of the two upper planes are combined to provide an independent measurement of the charge with an accuracy $\sigma_Z/Z = 4\%$ for helium. The pulse heights from the two lower planes are combined to provide another independent charge measurement with the same accuracy.

Helium nuclei traversing AMS were triggered as described in Ref. [32]. For each day, the trigger efficiency has been measured to be >81% over the entire rigidity range.

Monte Carlo (MC) simulated events were produced using a dedicated program developed by the collaboration based on the GEANT4-10.3 package [30]. The program simulates electromagnetic and hadronic [31] interactions of particles in the material of AMS and generates detector responses. The digitization of the signals is simulated precisely according to the measured characteristics of the electronics. The simulated events then undergo the same reconstruction as used for the data.

Event Selection.—AMS has collected 1.5×10^{11} cosmic ray events from May 20, 2011 to October 29, 2019. The collection time used in this analysis includes only those seconds during which the detector was in normal operating conditions and, in addition, AMS was pointing within 40° of the local zenith and the International Space Station was outside of the South Atlantic Anomaly. Because of the geomagnetic field, the daily collection time of the helium fluxes is $(4.5 - 7.5)\times10^3$ s at 2 GV, $(1.8 - 2.3)\times10^4$ s at 5 GV, $(3.3 - 3.8)\times10^4$ s at 10 GV, $(6.1 - 7.0)\times10^4$ s at 20 GV, and, above 30 GV, reaches $(6.7 - 7.3)\times10^4$ s out of

8.64×10^4 s per day.

The event selection is designed to minimize the total error. Helium events are required to be downward going and to have a reconstructed track in the inner tracker which passes through $L1$. This selection has an efficiency of $\sim 20\%$. Compared to Ref. [20], tracks are not required to pass through $L9$ leading to a five-fold increase in statistics for the helium sample. Track fitting quality criteria such as a χ^2/d.o.f. < 10 in the bending coordinate are applied. The five-fold increase in statistics, together with the improved understanding of systematic errors, leads to the improvement of accuracy.

Charge measurements on $L1$, the upper TOF, and the inner tracker are required to be compatible with charge $Z = 2$.

The measured rigidity is required to be greater than the local geomagnetic cutoff. The local geomagnetic cutoff was calculated directly from AMS data by measuring the helium and proton fluxes at each geomagnetic position. The details of this study will be included in a future publication [34]. To estimate the associated systematic error, we increase the calculated value of the geomagnetic cutoff by 10%. This results in a negligible (<0.4%) systematic error on the fluxes over the entire rigidity range. We have verified that using a geomagnetic cutoff derived from the most recent International Geomagnetic Reference Field (IGRF) model [35] with external non-symmetric magnetic fields [36] during the most geomagnetically disturbed periods does not introduce observable changes in the flux values nor in the systematic errors.

Because of the multiple independent measurements of the charge, the selected sample contains only a small contamination of particles which had $Z \neq 2$ at the top of the AMS. Comparing the proton and helium charge distributions in the inner tracker, the proton contamination of the helium sample was measured to be less than 0.01% over the entire rigidity range. The sample also contains helium from other nuclei which interact at the top of the AMS (for example, $L1$). This contribution was estimated to be below 0.1% for the entire rigidity range. The background contributions are subtracted from the flux and the uncertainties are accounted for in the systematic errors.

After selection, the event sample contains 7.6×10^8 helium nuclei.

TABLE SA. The range of each year from 2011 to 2019 in BRs and dates.

Year	Range [BR]	Range [Date]
2011	2426 – 2433	May 20, 2011 – December 16, 2011
2012	2434 – 2447	December 17, 2011 – December 28, 2012
2013	2448 – 2461	December 29, 2012 – January 10, 2014
2014	2462 – 2471	January 11, 2014 – September 29, 2014
2015	2473 – 2488	November 29, 2014 – January 9, 2016
2016	2489 – 2502	January 10, 2016 – January 21, 2017
2017	2503 – 2515	January 22, 2017 – January 7, 2018
2018	2516 – 2528	January 8, 2018 – December 24, 2018
2019	2529 – 2540	December 25, 2018 – October 29, 2019

Dip in 2017.—The dip in 2017 is most likely related to the burst of solar activity in the late declining phase of solar cycle 24. The burst started in July 2017 and culminated in a series of solar eruptions in September 2017 leading to a ground-level enhancement on September 10, 2017 (see https://gle.oulu.fi) and several Forbush decreases. This burst produced enhanced modulation of galactic cosmic rays during July-October 2017, observed as the dip.

Wavelet Analysis.—The continuous wavelet transform W_n of a time series x_n with equal time interval δt is defined as [40]:

$$W_n(s) = \sum_{n'=1}^{N} x_{n'} \psi^* \left[\frac{(n'-n)\delta t}{s} \right], \tag{S1}$$

where the $*$ indicates the complex conjugate of the wavelet function ψ, s is the period, and n is the time index of the wavelet. In this study, we chose the Morlet wavelet, consisting of a plane wave modulated by a Gaussian:

$$\psi(\eta) = \pi^{-1/4} e^{i6\eta} e^{-\eta^2/2}, \tag{S2}$$

where η is a nondimensional time parameter. The wavelet power is given by $|W_n(s)|^2$. The wavelet time-frequency power spectrum shows the temporal distribution of the power for each period s. The time-averaged power spectrum over a certain time interval is

$$\overline{W}_n^2(s) = \frac{1}{n_2 - n_1 + 1} \sum_{n=n_1}^{n_2} |W_n(s)|^2, \tag{S3}$$

where n_1 and n_2 are the beginning and ending indexes of the analyzed time interval, respectively.

In both the wavelet time-frequency power spectrum and time-averaged power spectrum, the normalized power is defined by the wavelet power divided by the variance σ^2 of the time series x_n in the corresponding time interval:

$$\sigma^2 = \frac{\sum_{n=n_1}^{n_2} (x_n - \overline{x})^2}{n_2 - n_1}, \tag{S4}$$

where $\overline{x}$ is the mean value of the time series. This normalization by variance is applied to show the strength of the periodicities.

To determine significance levels above which the power represents periodic structures, Monte Carlo simulations are used to assess the statistical significance against backgrounds which are generated by the lag-1 autoregressive process [40]:

$$y_n = \alpha y_{n-1} + z_n, \tag{S5}$$

where z_n is a Gaussian with zero mean and width such that the variance of the simulated time series is equal to the measured time series. Here, α is the lag-1 autocorrection obtained from the measured time series x_n:

$$\alpha = \frac{\sum_{n=1}^{N-1} (x_n - \overline{x})(x_{n+1} - \overline{x})}{\sum_{n=1}^{N} (x_n - \overline{x})^2}, \tag{S6}$$

where N is the number of measured points and $\overline{x}$ is the mean value of the time series.

For each period, the 95% confidence level is determined by the power exceeded by 5% of the power values calculated from the simulated background. The 95% confidence level has different shapes due to different solar modulation effects as a function of rigidity.

To examine the relation between time series X_n and Y_n, the cross wavelet transform (XWT) [42] for each period s is calculated as

$$W_n^{XY}(s) = \frac{W_n^X(s) W_n^{Y*}(s)}{\sigma_X \sigma_Y}, \tag{S7}$$

where σ_X and σ_Y are the standard deviations of the time series X_n and Y_n, respectively. The XWT exposes regions in time-frequency space with high common normalized power.

Interplanetary Space Environment.—The intensity variations of cosmic rays are caused by the temporal evolution of the interplanetary space environment. In particular, the solar wind speed is related to cosmic-ray advection, the variation of solar wind proton density is related to cosmic-ray adiabatic energy changes, and the interplanetary magnetic field is related to cosmic-ray diffusion and drifts [1]. Figure S18 shows the wavelet time-frequency power spectra of the daily averages of these interplanetary space environment properties [41] in 2016. See also Fig. S18 in Ref. [18]. To investigate their relations with the observed periodicities in Φ_{He}, the cross wavelet transform [42] is performed as shown in Fig. S19. As seen, the Φ_{He} are observed to be related to the interplanetary space environment properties for all periodicities, such as the radial component (along the Sun-Earth direction) of the interplanetary magnetic field for the 9-day periodicity and the solar wind speed for the 13.5-day periodicity.

Hysteresis Analysis.—The hysteresis occurs over the time span from 2011 to 2015 as seen in Fig. S23 and Fig. 4. To analyze the significance of the hysteresis, we select the two time intervals with the same Φ_{He}, one before 2014 and one after, with the most significant difference in $\Phi_{\mathrm{He}}/\Phi_p$. This minimizes the systematic errors such as the error from unfolding. From this, we determine that the maximum difference for [1.71–1.92] GV is at $\Phi_{\mathrm{He}} = 69[\mathrm{m}^{-2} \cdot \mathrm{s}^{-1} \cdot \mathrm{sr}^{-1} \cdot \mathrm{GV}^{-1}]$ which occurs in 2012 and in 2015. The significance of the difference is 5.5σ, see Fig. S23(a). The analysis is repeated for other rigidity bins, see Fig. S23(b)-(f).

To obtain the overall significance of the hysteresis, we repeat the procedure for remaining non-overlapping time intervals and determine that the maximum difference for [1.71–1.92] GV is at $\Phi_{\mathrm{He}} = 50[\mathrm{m}^{-2} \cdot \mathrm{s}^{-1} \cdot \mathrm{sr}^{-1} \cdot \mathrm{GV}^{-1}]$ which occurs in 2013 and in 2014. The significance of the difference is 1.6σ, see Fig. S23(a). The total significance is 5.9σ by combining the significances at two Φ_{He} values. The analysis is repeated for other rigidity bins, see Fig. S23(b)-(f).

As seen from Fig. S23(a)-(c), below 2.4 GV the combined significance is greater than 7σ.

The same analysis is performed on daily $\Phi_{\mathrm{He}}/\Phi_p$ as a function of daily Φ_p as shown in Fig. S26.

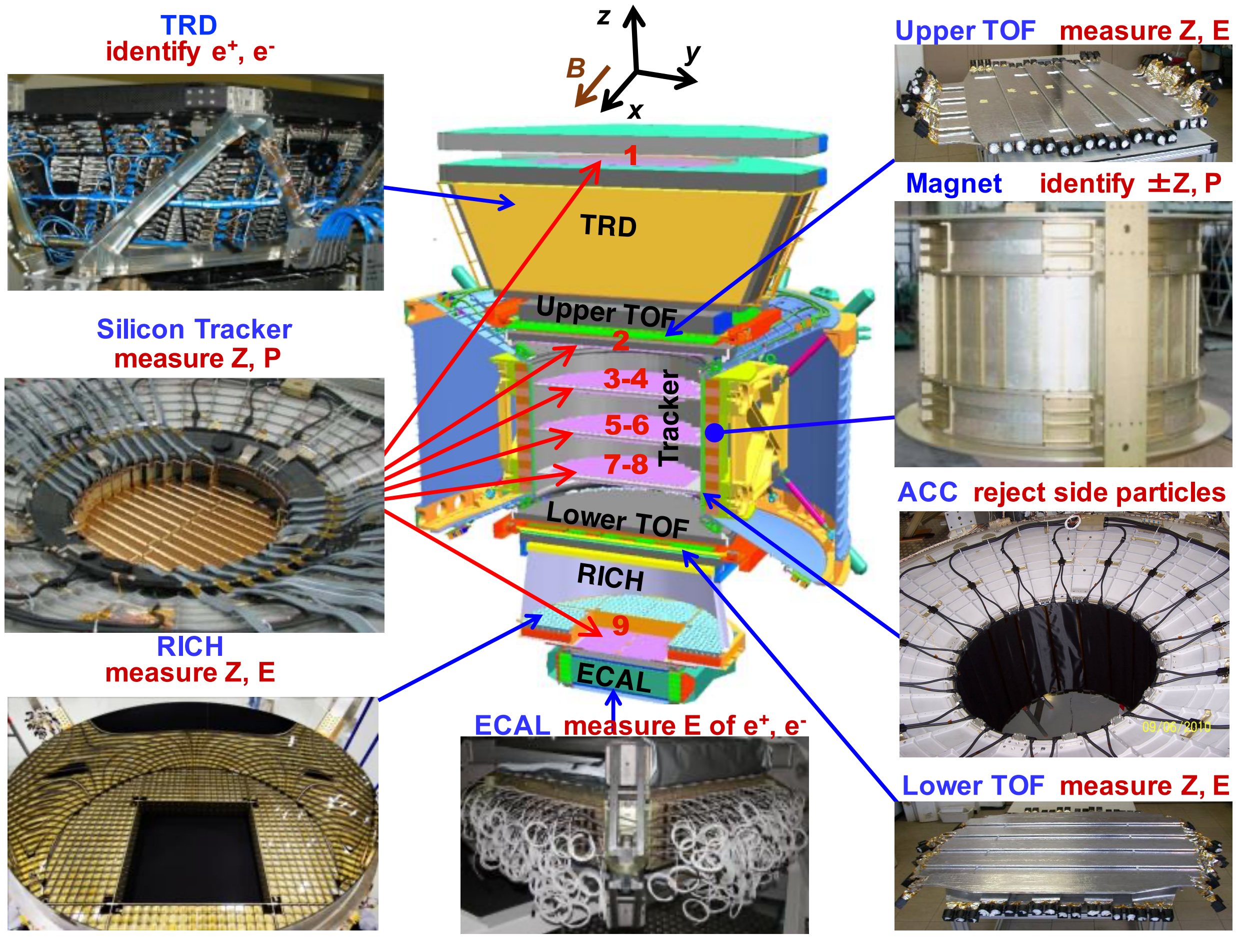

FIG. S1. The AMS detector showing the main elements and their functions. AMS is a TeV precision, multipurpose particle physics magnetic spectrometer in space. It identifies particles and nuclei by their charge Z, energy E, and momentum P or rigidity ($R = P/Z$), which are measured independently by the Tracker, TOF, RICH and ECAL. The ACC counters, located in the magnet bore, are used to reject particles entering AMS from the side. The AMS coordinate system is also shown. The x axis is parallel to the main component of the magnetic field and the z axis points vertically with $z = 0$ at the center of the magnet.

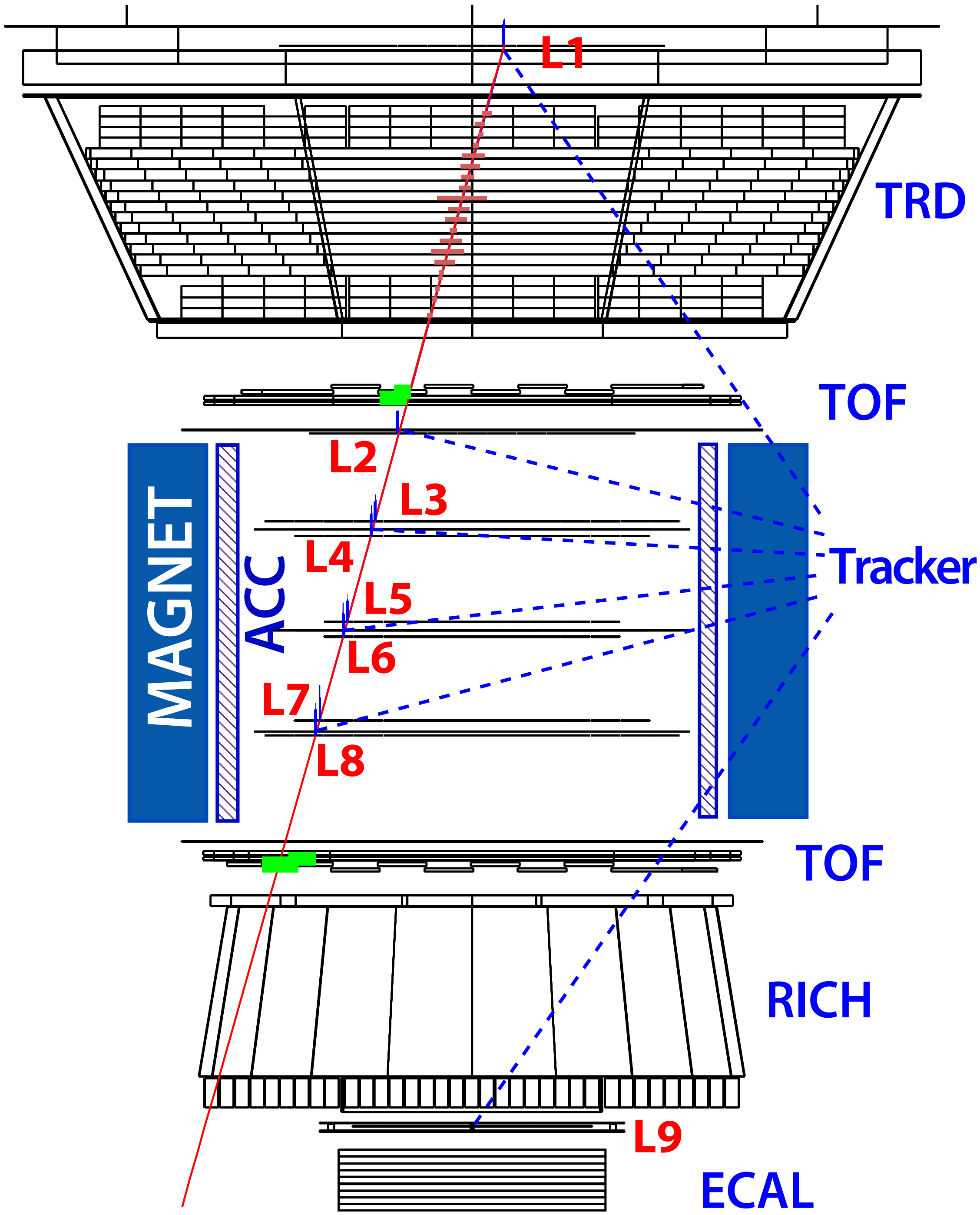

FIG. S2. A helium event display in the bending plane. The red line indicates the reconstructed trajectory. The magenta spread in TRD shows the dE/dx measurements in different TRD layers, green areas in upper and lower TOF carry the information of the dE/dx as well as the coordinate and time measurements. The vertical blue lines in the tracker layers carry the information of coordinates and dE/dx or pulse heights. This downward-going event is identified as a helium nucleus ($Z = 2$) with $R = 4.16$ GV.

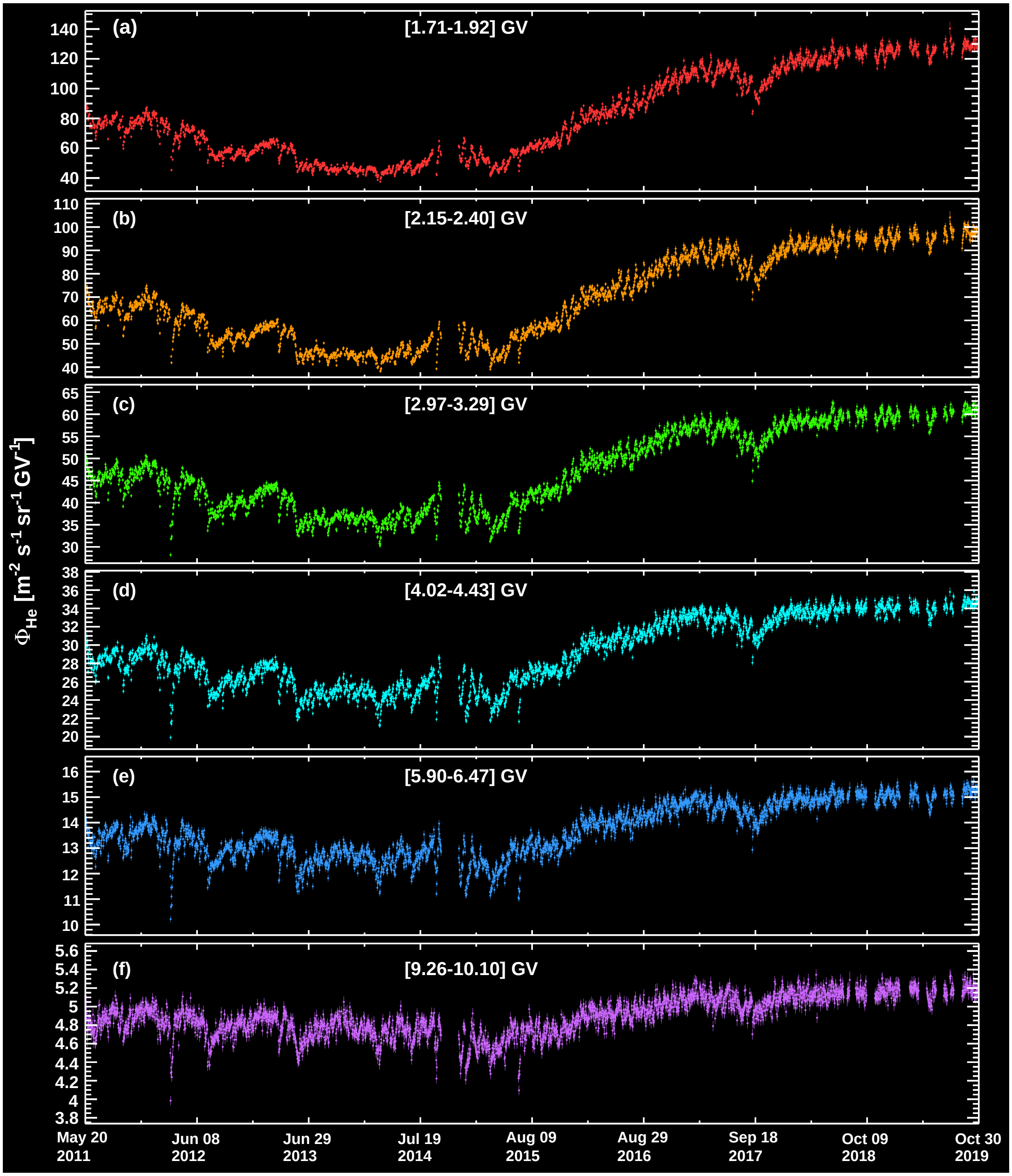

FIG. S3. Figure 1 in rectangular format. The daily AMS helium fluxes Φ_{He} for the rigidity bins (a) [1.71 – 1.92] GV, (b) [2.15 – 2.40] GV, (c) [2.97 – 3.29] GV, (d) [4.02 – 4.43] GV, (e) [5.90 – 6.47] GV, and (f) [9.26 – 10.10] GV measured from May 20, 2011 to October 29, 2019 which includes a major portion of solar cycle 24 (from December 2008 to December 2019). The AMS data cover the ascending phase, the maximum, and descending phase to the minimum of solar cycle 24. Days with SEPs are removed for the two lowest rigidity bins shown. The gaps in the fluxes are due to detector studies and upgrades. As seen, Φ_{He} exhibit large variations with time, and the relative magnitude of these variations decreases with increasing rigidity.

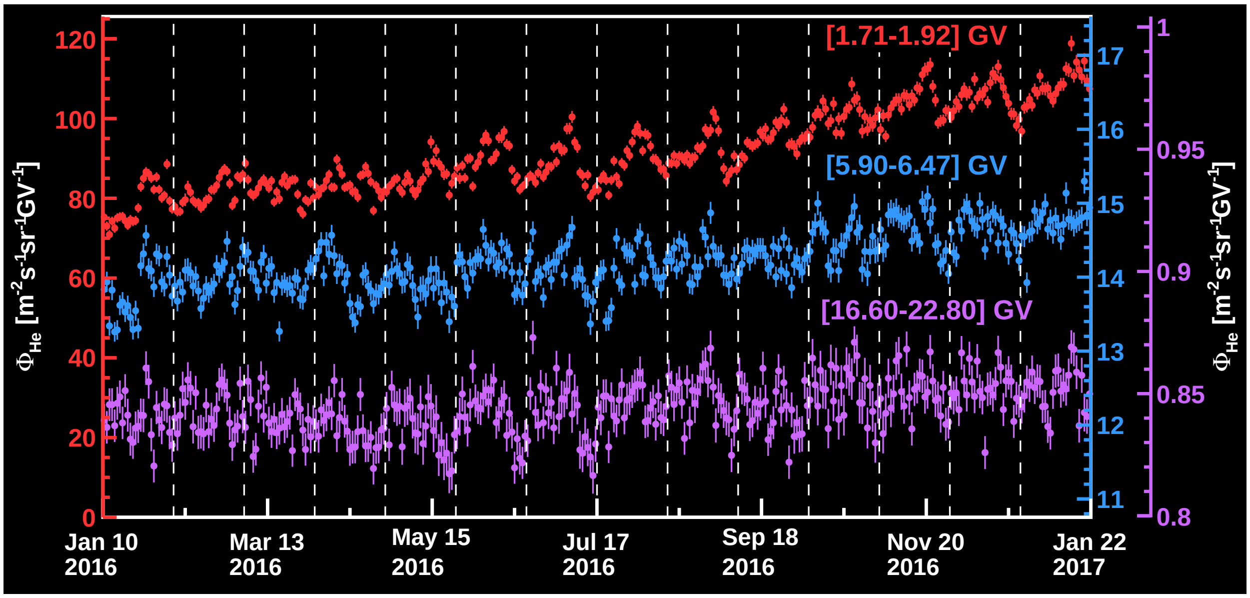

FIG. S4. The daily helium fluxes Φ_{He} measured in 2016 for three rigidity bins. Vertical dashed lines separate Bartels rotations. As seen, double-peak and triple-peak structures are visible in different Bartels rotations. The different colors in three vertical scales correspond to different rigidities.

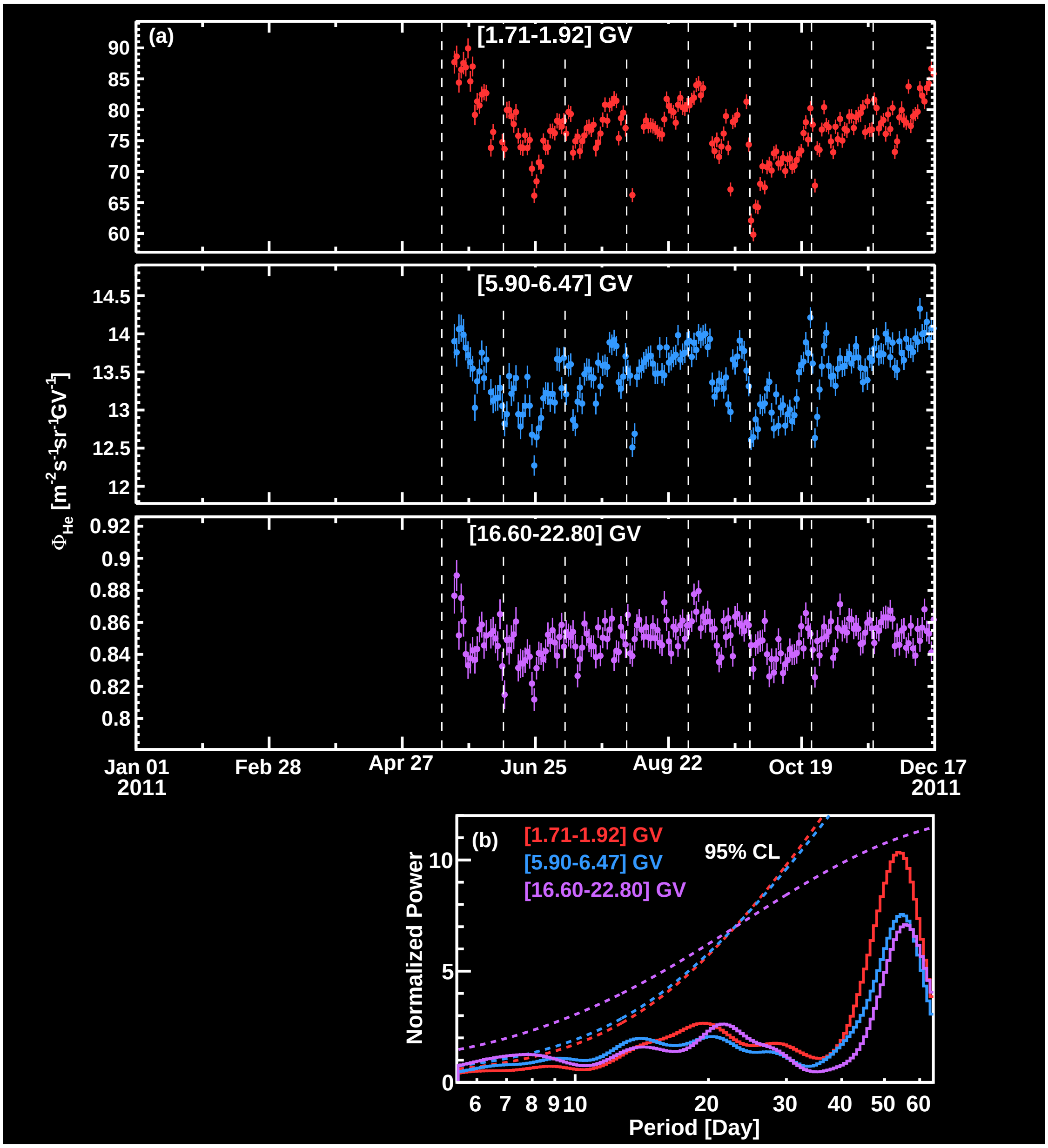

FIG. S5. (a) The daily AMS helium fluxes Φ_{He} measured from May 20, 2011 to December 16, 2011 for three rigidity bins. Vertical dashed lines separate Bartels rotations. (b) Wavelet normalized power spectra for the three rigidity bins. Dashed colored curves indicate the 95% confidence levels for the three rigidity bins.

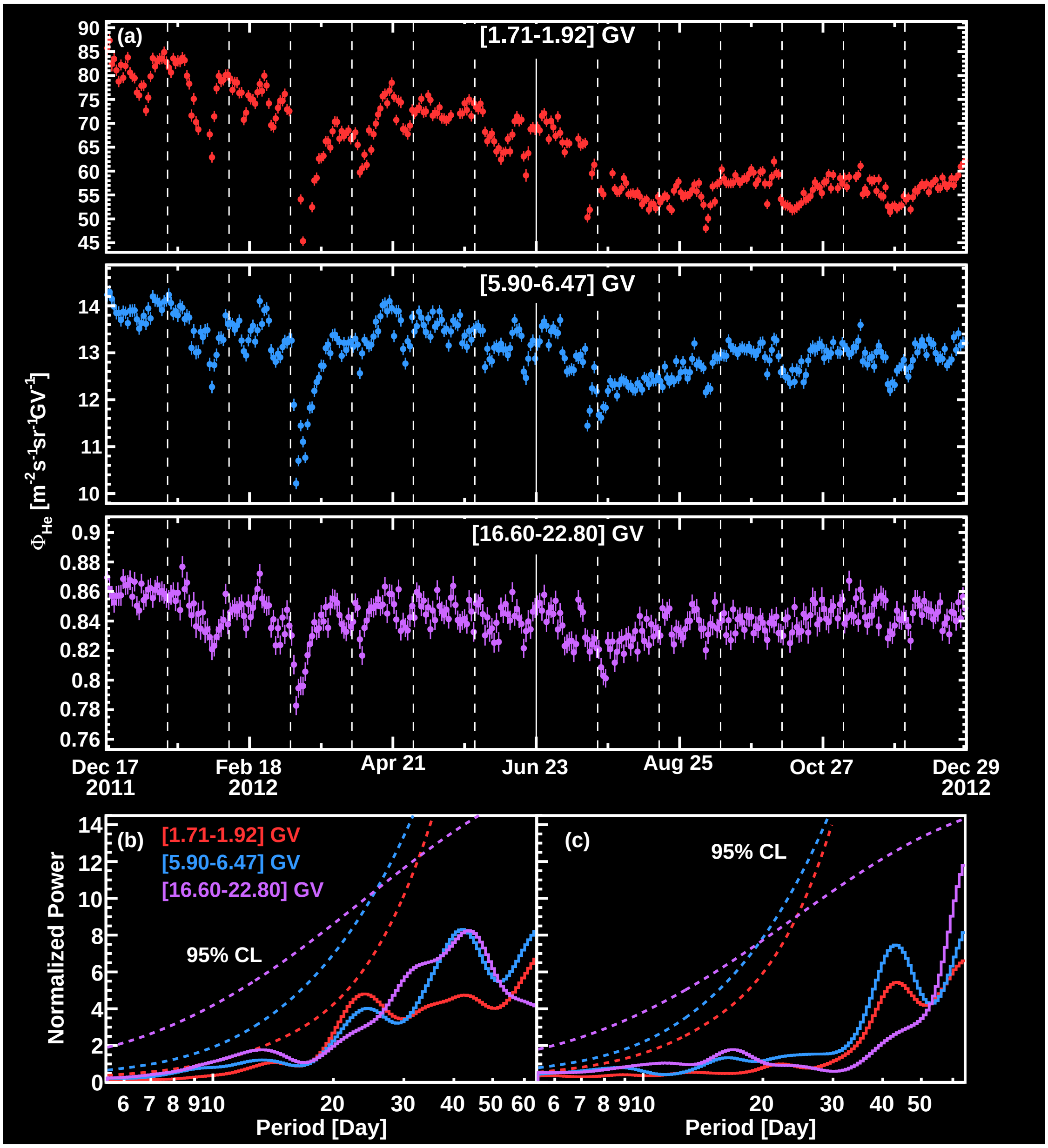

FIG. S6. (a) The daily AMS helium fluxes Φ_{He} measured from December 17, 2011 to December 28, 2012 for three rigidity bins. Vertical dashed lines separate Bartels rotations. The vertical solid line separates two equal time intervals where the power spectra are calculated. (b,c) Wavelet normalized power spectra for the three rigidity bins averaged (b) from December 17, 2011 to June 22, 2012 and (c) from June 23, 2012 to December 28, 2012. Dashed colored curves indicate the 95% confidence levels for the three rigidity bins.

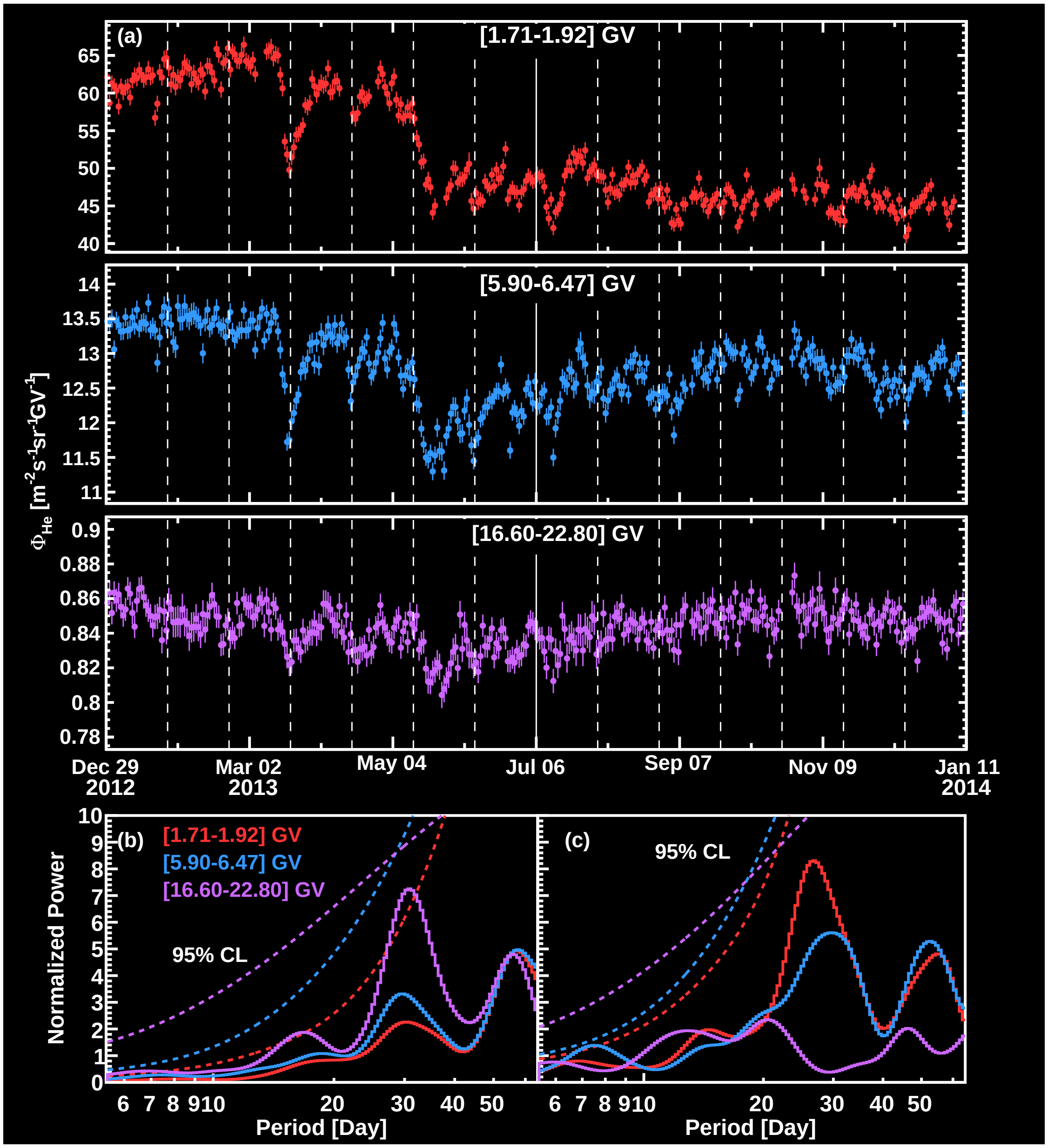

FIG. S7. (a) The daily AMS helium fluxes Φ_{He} measured from December 29, 2012 to January 10, 2014 for three rigidity bins. Vertical dashed lines separate Bartels rotations. The vertical solid line separates two equal time intervals where the power spectra are calculated. (b,c) Wavelet normalized power spectra for the three rigidity bins averaged (b) from December 29, 2012 to July 5, 2013 and (c) from July 6, 2013 to January 10, 2014. Dashed colored curves indicate the 95% confidence levels for the three rigidity bins.

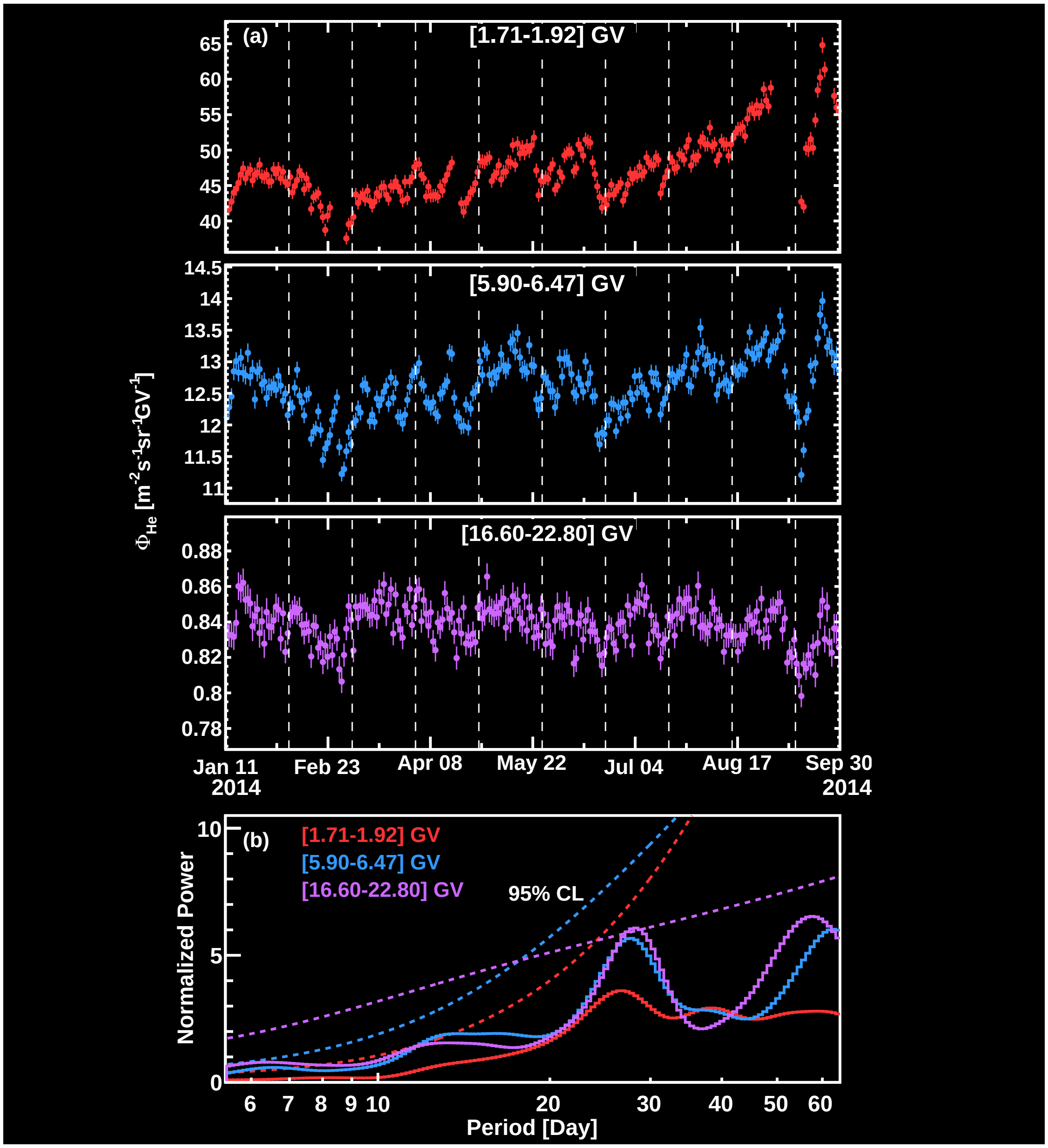

FIG. S8. (a) The daily AMS helium fluxes Φ_{He} measured from January 11, 2014 to September 29, 2014 for three rigidity bins. Vertical dashed lines separate Bartels rotations. (b) Wavelet normalized power spectra for the three rigidity bins. Dashed colored curves indicate the 95% confidence levels for the three rigidity bins. Note that in the time interval from September 30, 2014 to November 28, 2014, AMS was performing detector studies.

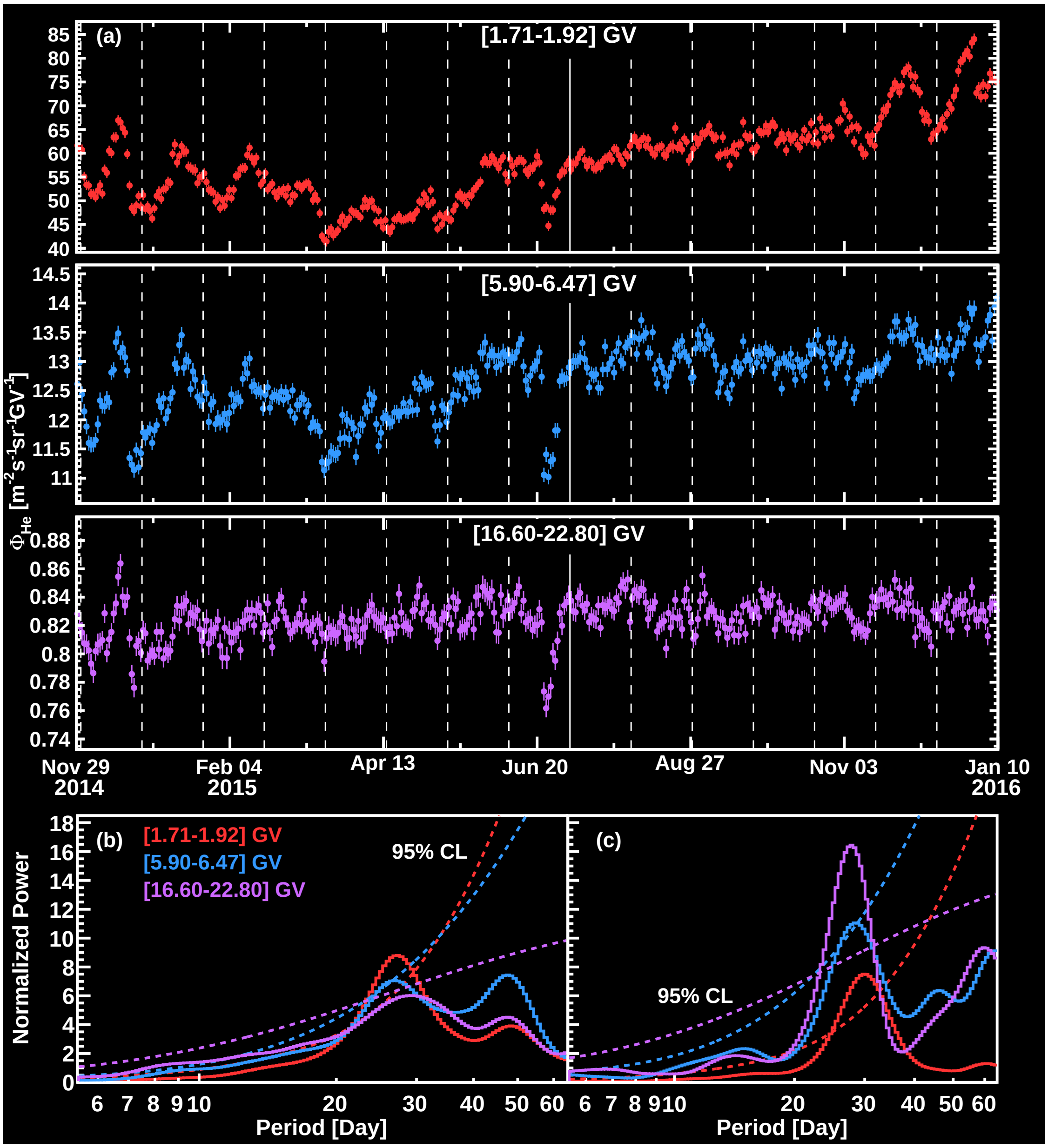

FIG. S9. (a) The daily AMS helium fluxes Φ_{He} measured from November 29, 2014 to January 9, 2016 for three rigidity bins. Vertical dashed lines separate Bartels rotations. The vertical solid line separates two approximately equal time intervals where the power spectra are calculated. (b,c) Wavelet normalized power spectra for the three rigidity bins averaged (b) from December 1, 2014 to July 4, 2015 and (c) from July 5, 2015 to January 9, 2016. Dashed colored curves indicate the 95% confidence levels for the three rigidity bins.

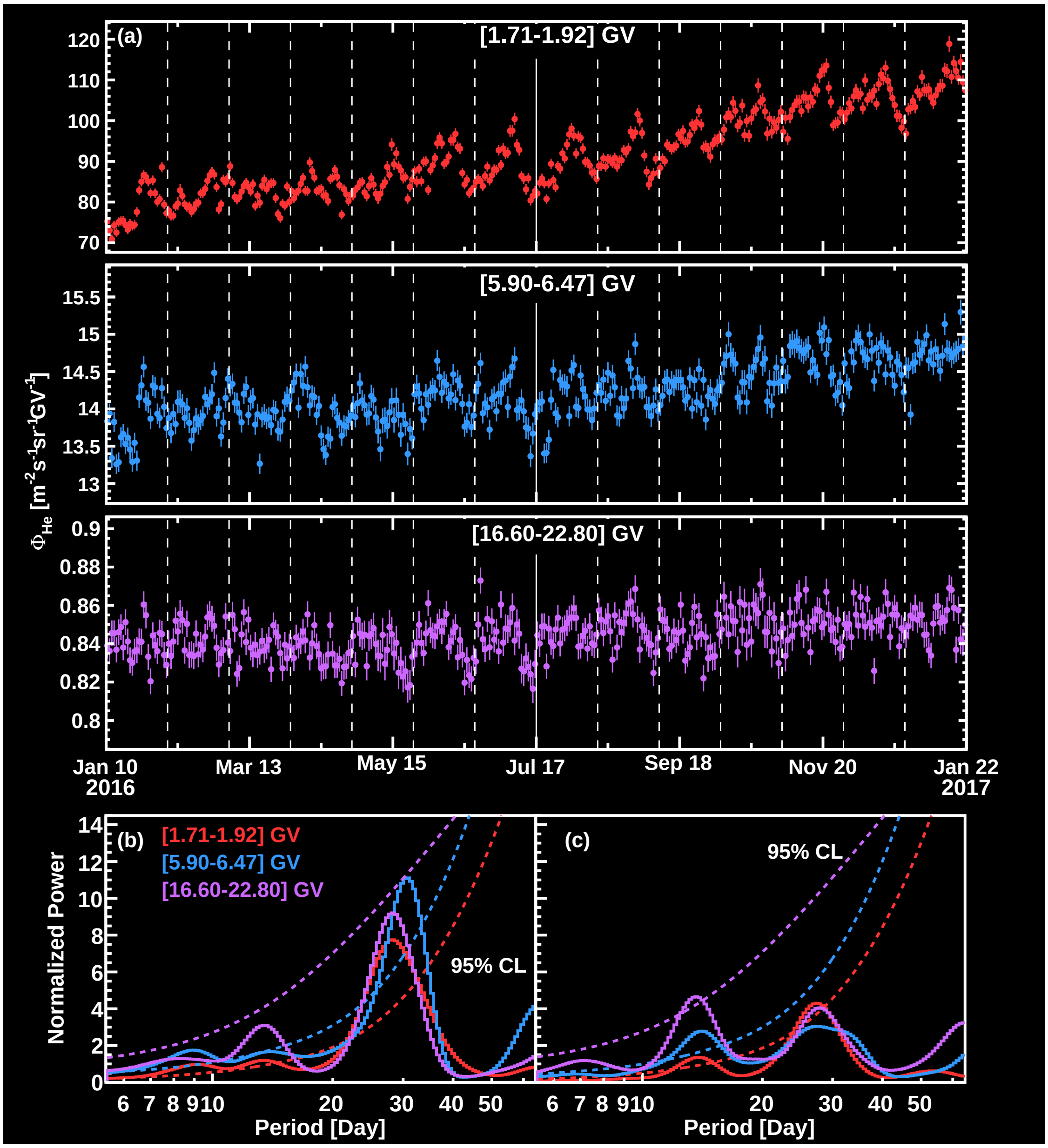

FIG. S10. (a) The daily AMS helium fluxes Φ_{He} measured from January 10, 2016 to January 21, 2017 for three rigidity bins. Vertical dashed lines separate Bartels rotations. The vertical solid line separates two equal time intervals where the power spectra are calculated. (b,c) Wavelet normalized power spectra for the three rigidity bins averaged (b) from January 10, 2016 to July 16, 2016 and (c) from July 17, 2016 to January 21, 2017. Dashed colored curves indicate the 95% confidence levels for the three rigidity bins. See text for further discussion.

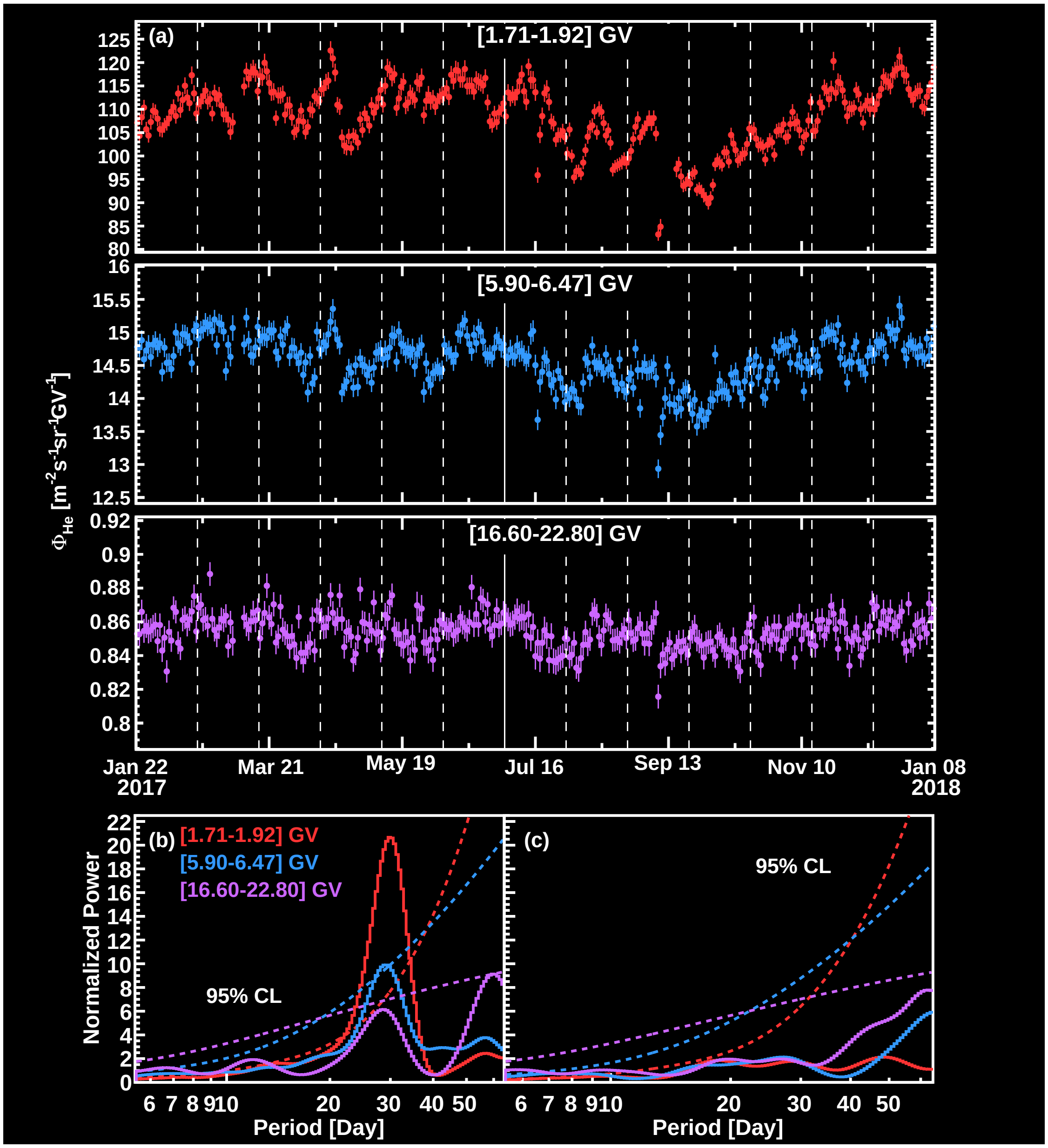

FIG. S11. (a) The daily AMS helium fluxes Φ_{He} measured from January 22, 2017 to January 7, 2018 for three rigidity bins. Vertical dashed lines separate Bartels rotations. The vertical solid line separates two approximately equal time intervals where the power spectra are calculated. (b,c) Wavelet normalized power spectra for the three rigidity bins averaged (b) from January 22, 2017 to July 2, 2017 and (c) from July 3, 2017 to January 7, 2018. Dashed colored curves indicate the 95% confidence levels for the three rigidity bins.

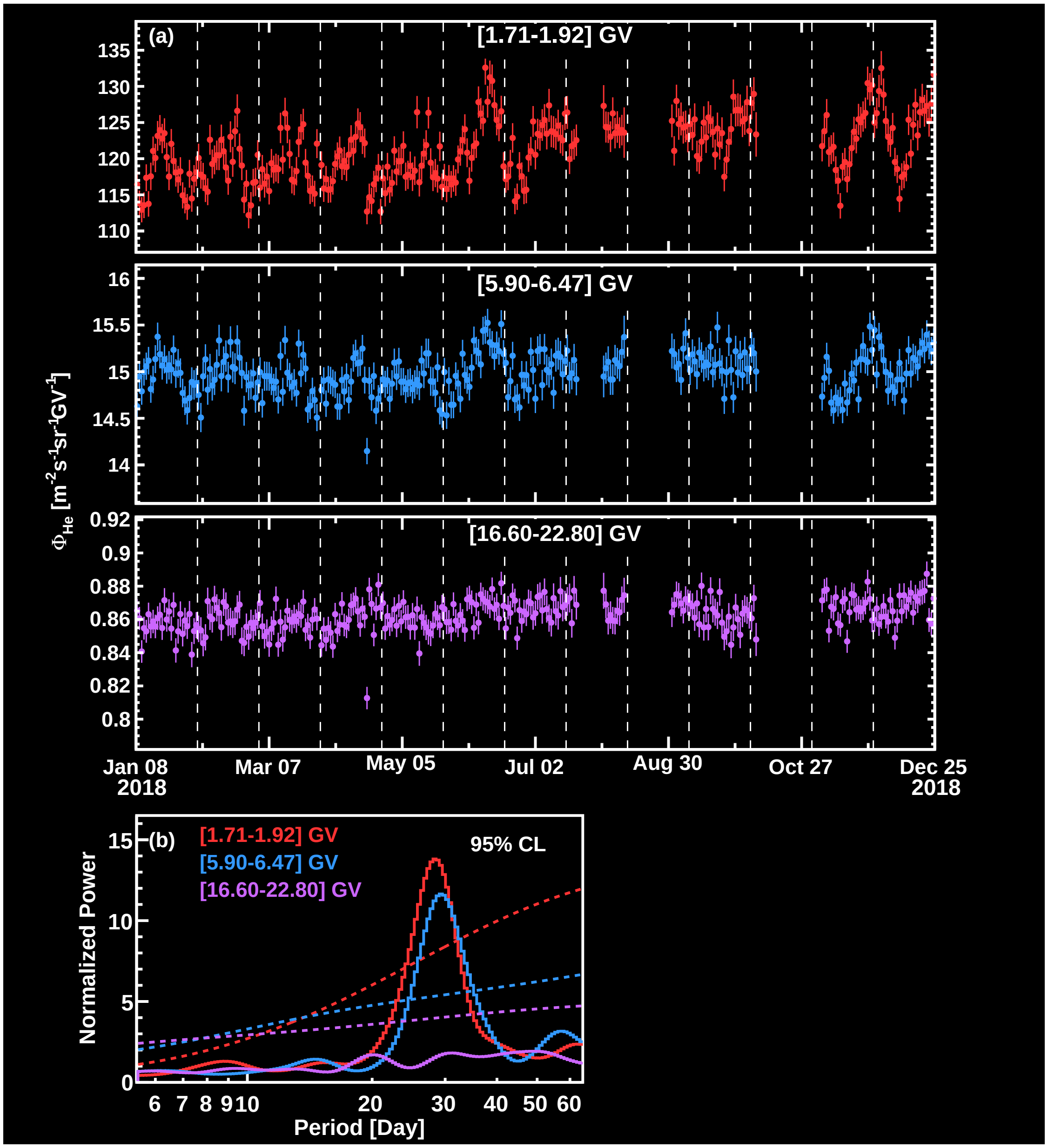

FIG. S12. (a) The daily AMS helium fluxes Φ_{He} measured from January 8, 2018 to December 24, 2018 for three rigidity bins. Vertical dashed lines separate Bartels rotations. (b) Wavelet normalized power spectra for the three rigidity bins averaged from January 8, 2018 to July 20, 2018. Dashed colored curves indicate the 95% confidence levels for the three rigidity bins. Due to AMS upgrade, the data after July 20, 2018 is not continuous. Therefore, it is not included in the periodicity analysis.

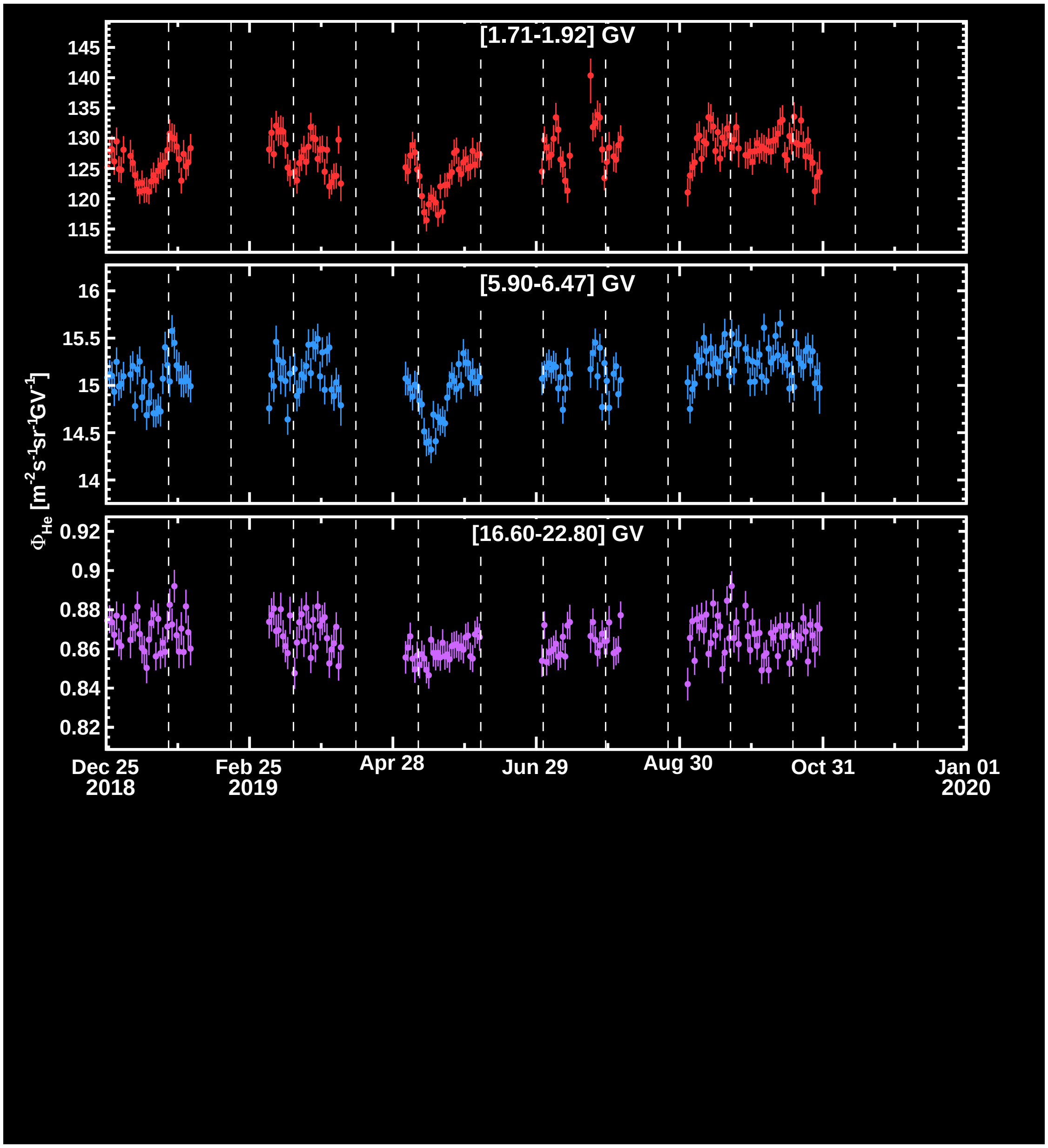

FIG. S13. The daily AMS helium fluxes Φ_{He} measured from December 25, 2018 to October 29, 2019 for three rigidity bins. Vertical dashed lines separate Bartels rotations. Due to AMS upgrade, the 2019 data is not continuous. Therefore it is not included in the periodicity analysis.

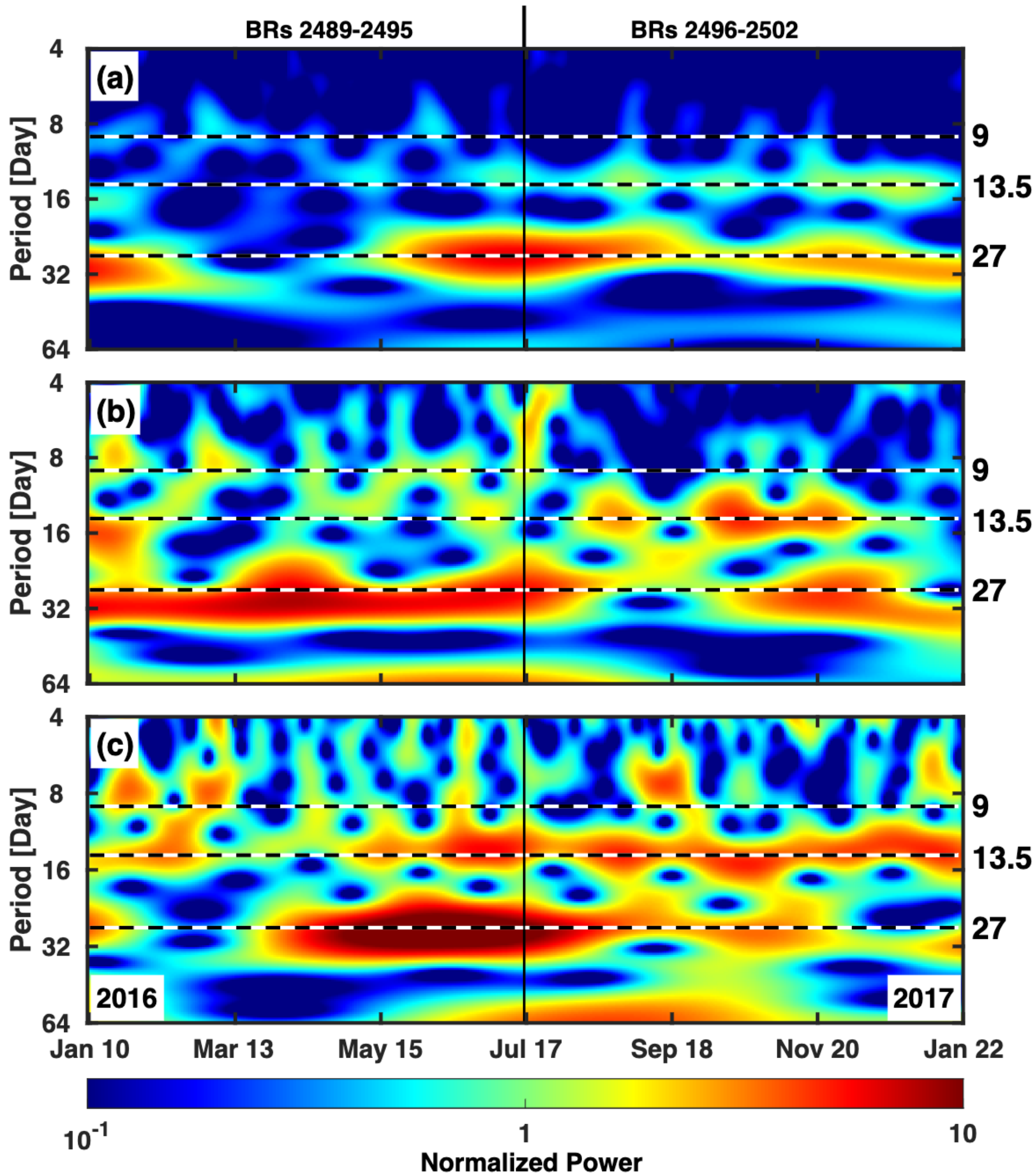

FIG. S14. The wavelet time-frequency power spectrum of daily AMS helium fluxes from January 10, 2016 to January 21, 2017 for the rigidity bins (a) [1.71 – 1.92] GV, (b) [5.90 – 6.47] GV, and (c) [16.60 – 22.80] GV. The color code at the bottom of the figure indicates the normalized power. The vertical scales are in decreasing period (increasing frequency). As seen, periods of 9, 13.5, and 27 days are observed. The strength of all three periodicities changes with time and rigidity. In particular, shorter periods of 9 and 13.5 days, when present, are more visible at [5.90–6.47] GV and [16.60–22.80] GV compared to [1.71–1.92] GV. The horizontal dashed lines indicate the locations of 9-day, 13.5-day, and 27-day periods shown on the right scale. The vertical solid line indicates the boundary of the two time intervals marked on the top. At [5.90–6.47] GV, the first time interval (BRs 2489–2495) is when the 9-day period is visible; the second time interval (BRs 2496–2502) is when the 9-day period is not visible.

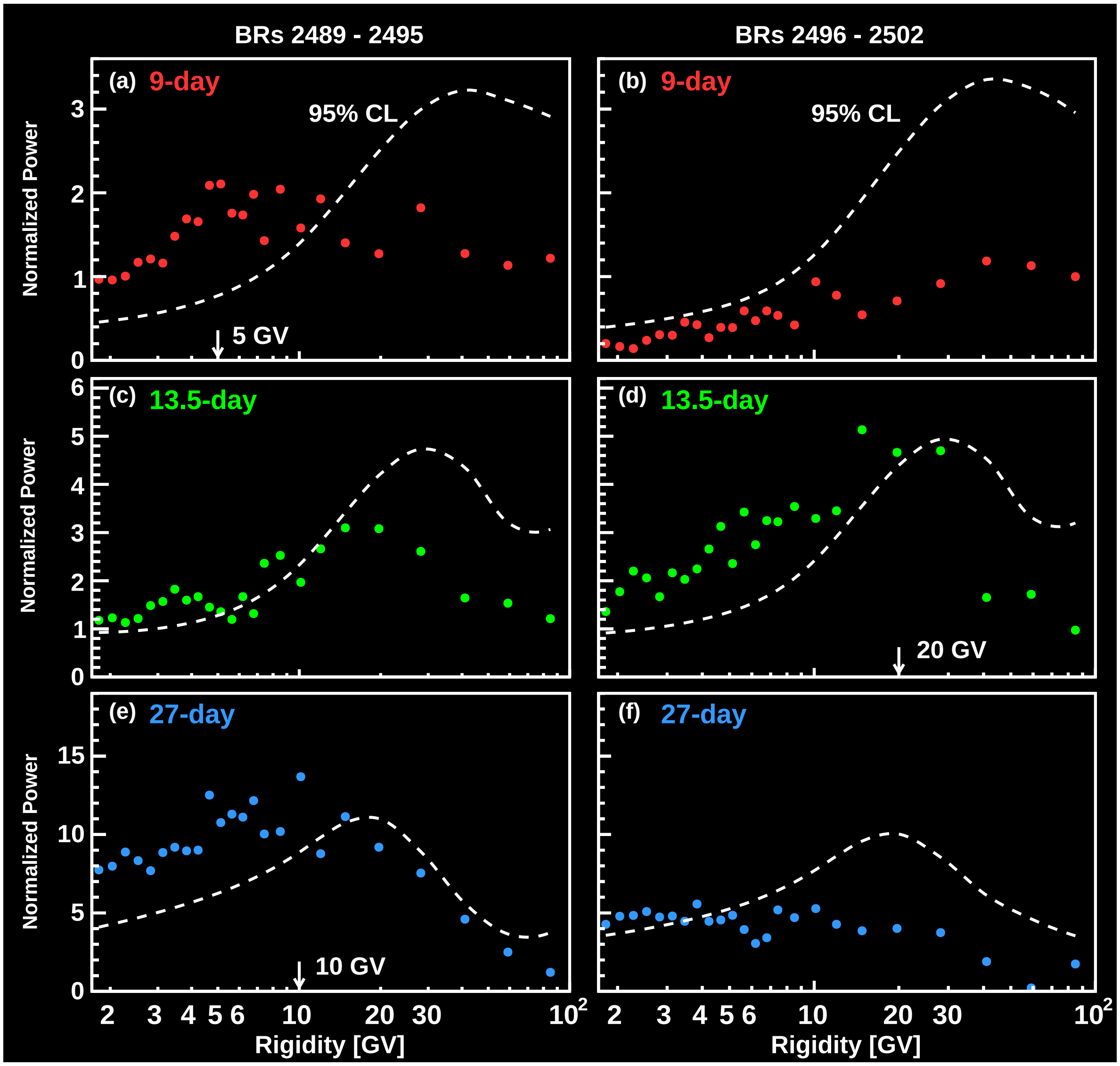

FIG. S15. The peak values of the normalized power around (a,b) 9 days, (c,d) 13.5 days, and (e,f) 27 days as a function of rigidity for (a,c,e) the first and (b,d,f) the second time intervals in 2016. Dashed curves indicate the 95% confidence levels. As seen, the strength of all three periodicities is rigidity dependent. In particular, as shown in (a), the strength of 9-day periodicity increases with increasing rigidity up to $\sim$ 5 GV; as shown in (d), the strength of 13.5-day periodicity increases with increasing rigidity up to $\sim$ 20 GV; and as shown in (e), the strength of 27-day periodicity increases with increasing rigidity up to $\sim$ 10 GV.

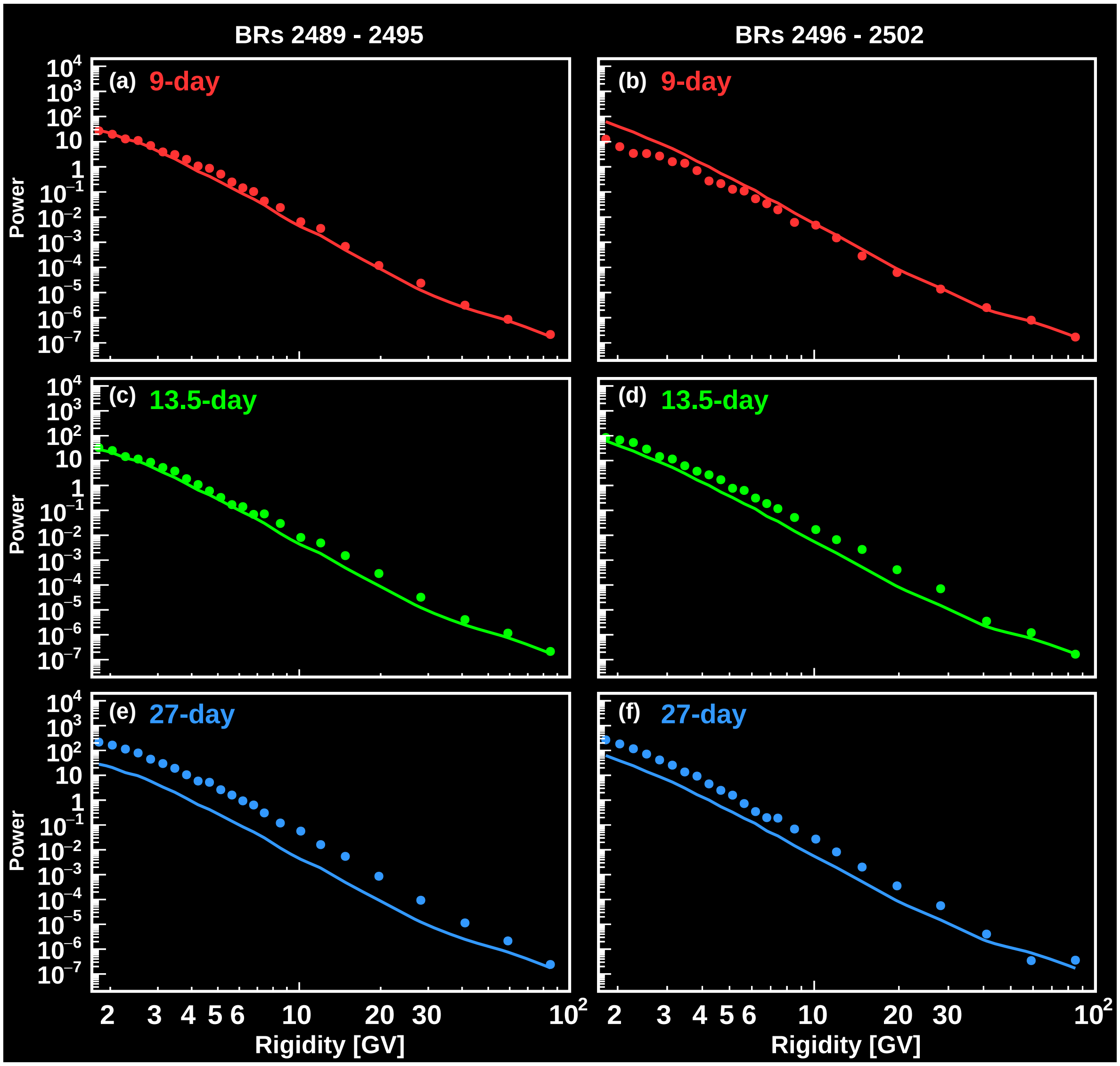

FIG. S16. The peak values of the unnormalized power (colored points) in units of flux-squared around (a,b) 9 days, (c,d) 13.5 days, and (e,f) 27 days as a function of rigidity, for (a,c,e) the first and (b,d,f) the second time intervals in 2016. Solid colored curves indicate the rigidity dependence of the flux variance in the corresponding time interval. As seen, both the unnormalized power of these periodicities and the flux variance in the two time intervals decrease with increasing rigidity.

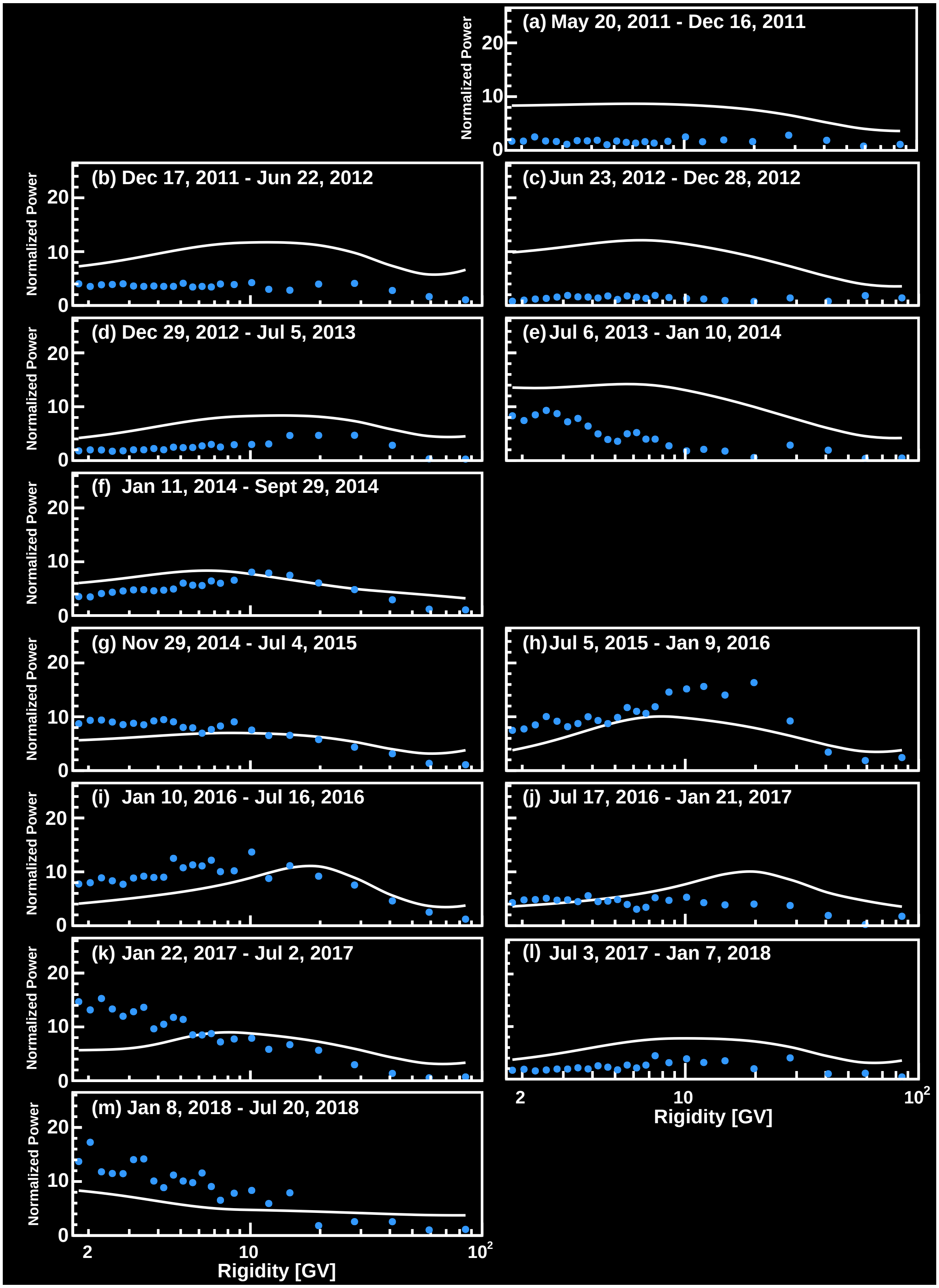

FIG. S17. The peak values of normalized power around 27 days (blue points) as a function of rigidity for time intervals from 2011 to 2018. The curves indicate the 95% confidence levels. As seen, the 27-day periodicity only becomes significant from 2014 to 2018, and its rigidity dependence varies in different time intervals.

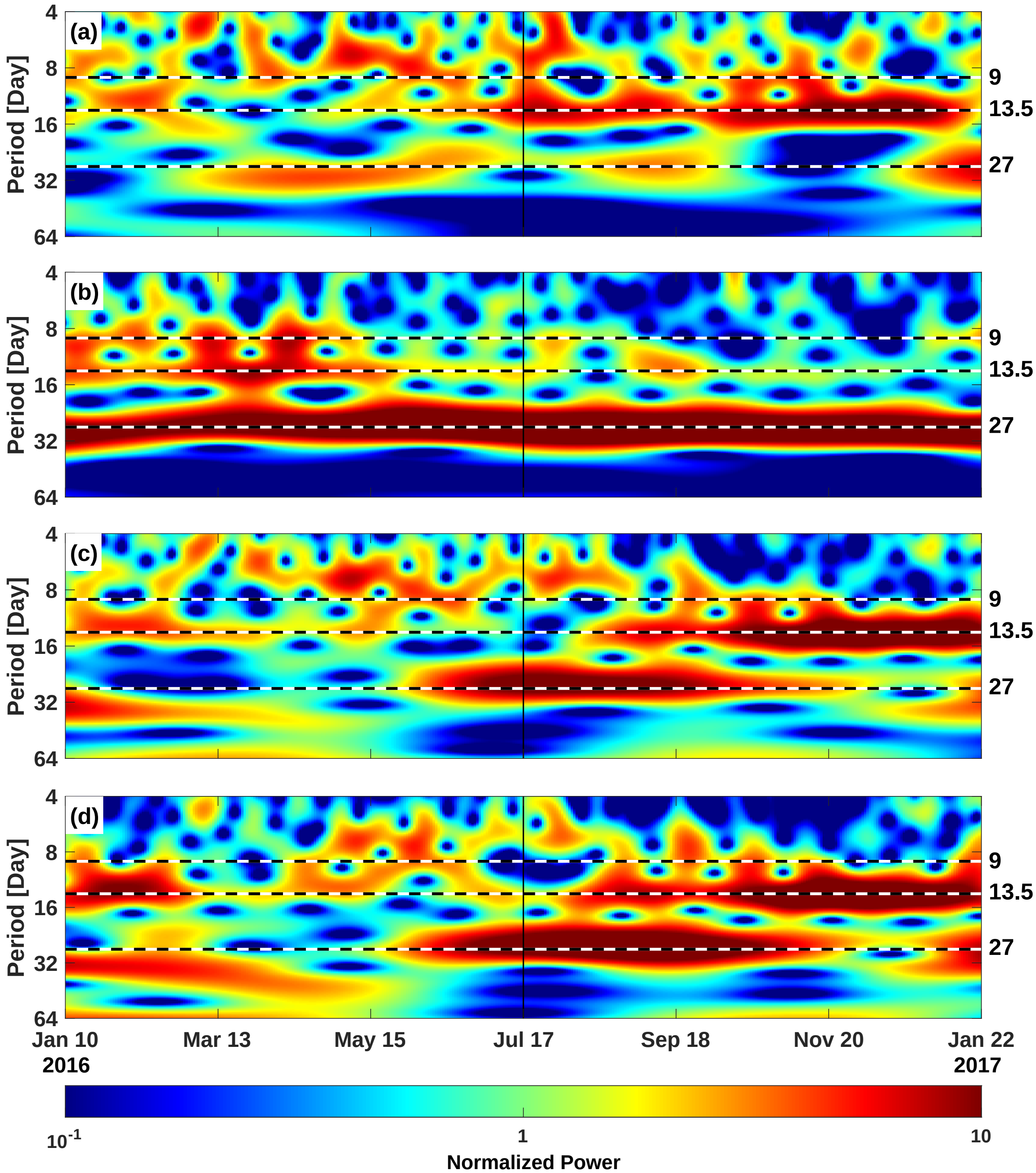

FIG. S18. The wavelet time-frequency power spectrum in 2016 of the daily averages of the local (a) interplanetary magnetic field magnitude, (b) radial component (along the Sun-Earth direction) of the interplanetary magnetic field, (c) solar wind proton density, and (d) solar wind speed. These data are obtained from Ref. [41]. The color code at the bottom of the figure indicates the normalized power. The horizontal dashed lines indicate the locations of 9-day, 13.5-day, and 27-day periods shown on the right scale. The vertical solid lines indicate the boundaries of the two time intervals.

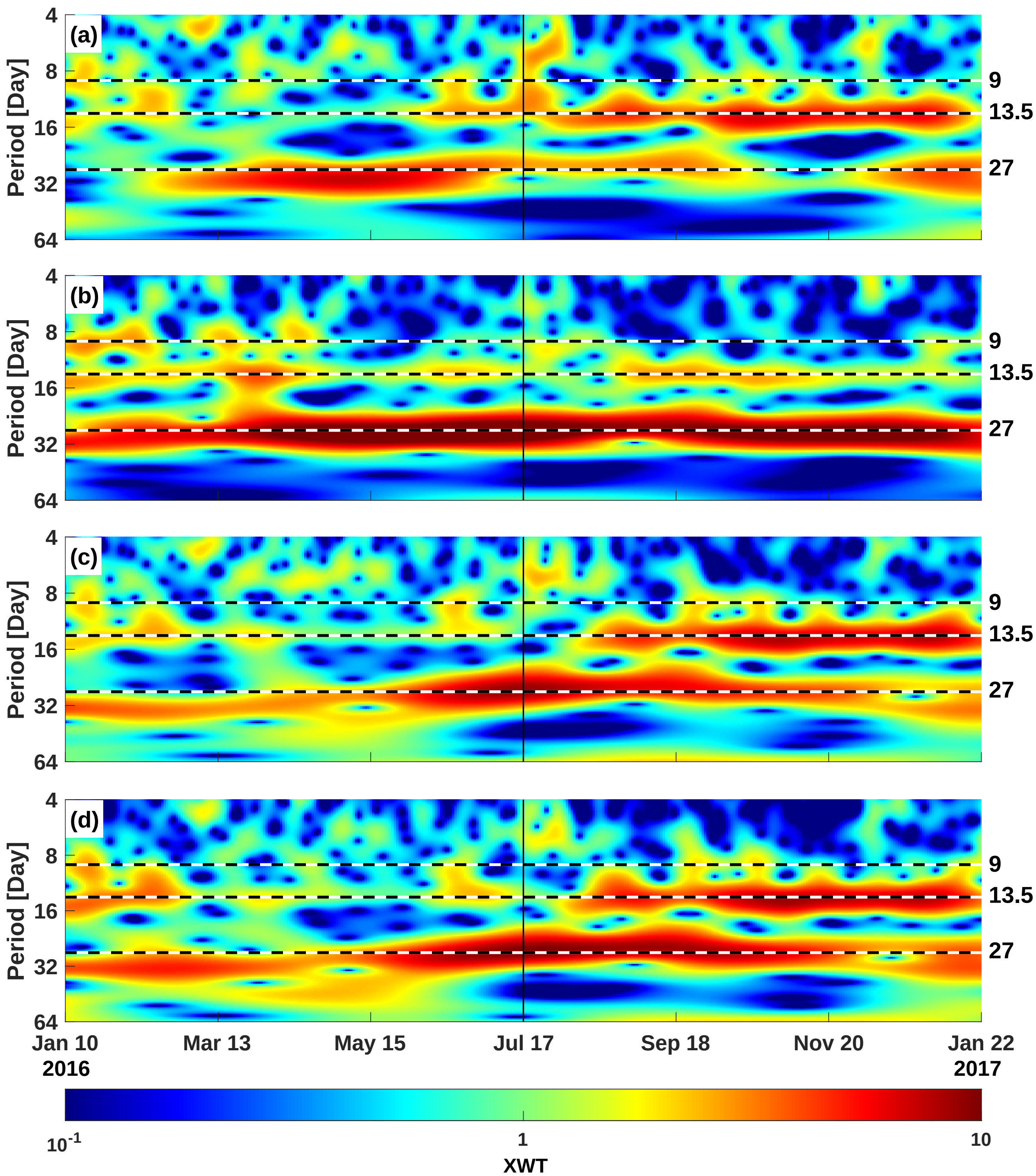

FIG. S19. Cross wavelet transformation (XWT) between the daily averages of the local (a) interplanetary magnetic field magnitude, (b) radial component (along the Sun-Earth direction) of the interplanetary magnetic field, (c) solar wind proton density, and (d) solar wind speed and daily AMS helium fluxes at [9.26–10.10] GV in 2016. The color code indicates the values of XWT. The horizontal dashed lines indicate the locations of 9-day, 13.5-day, and 27-day periods shown on the right scale. The vertical solid lines indicate the boundaries of the two time intervals. The helium fluxes are observed to be related to interplanetary space environment properties for all periodicities, see for example in (b) the radial component of the interplanetary magnetic field for the 9-day periodicity and in (d) the solar wind speed for the 13.5-day periodicity.

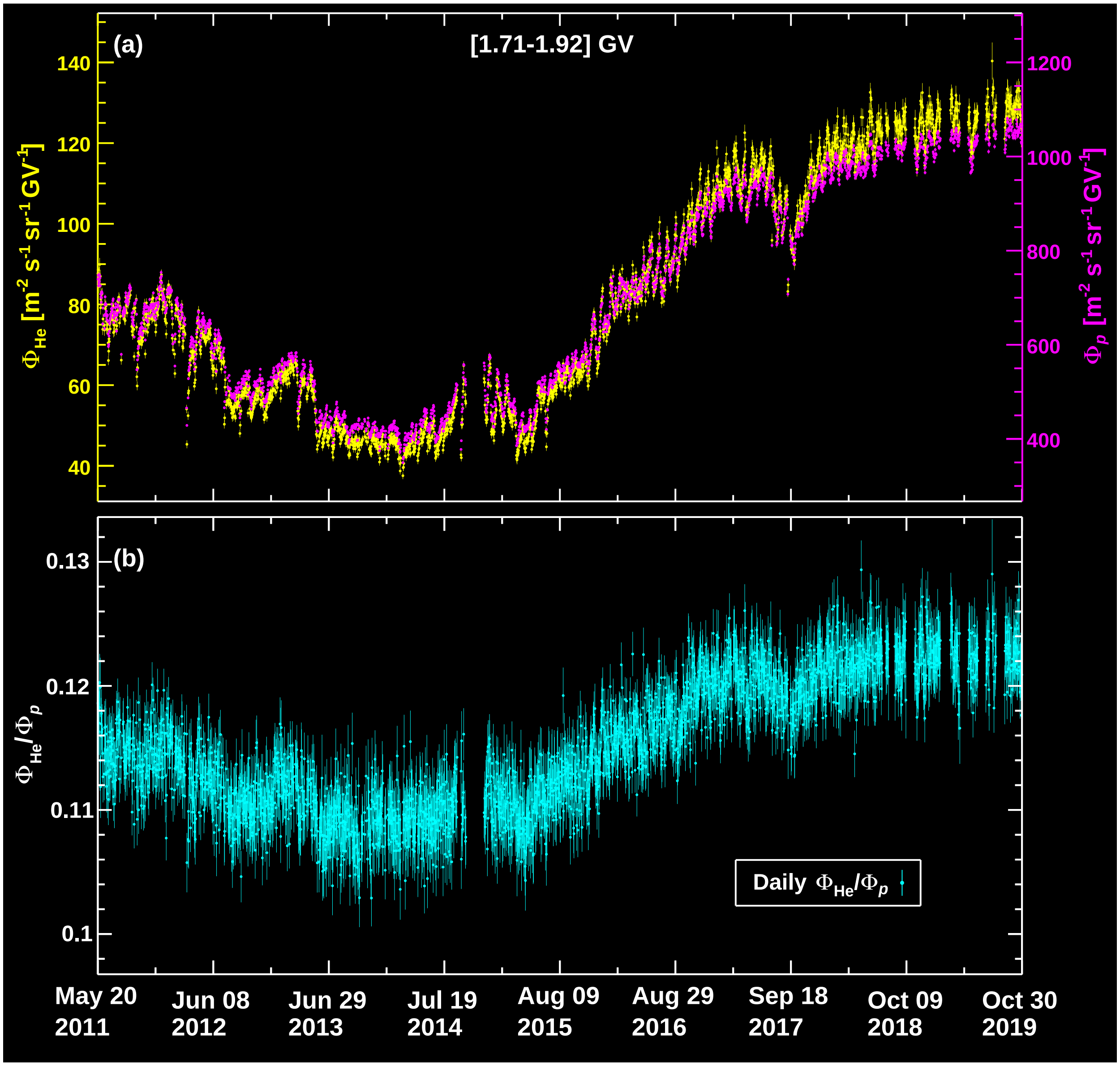

FIG. S20. (a) Φ_{He} (yellow) and Φ_p (magenta) and (b) $\Phi_{\mathrm{He}}/\Phi_p$ (cyan) measured from May 20, 2011 to October 29, 2019 at [1.71 – 1.92] GV. As seen in (b), $\Phi_{\mathrm{He}}/\Phi_p$ reaches a minimum in 2013 – 2014, when the fluxes are also in their minima, and a maximum in 2018 – 2019, when the fluxes are also in their maxima, see (a). In 2017, $\Phi_{\mathrm{He}}/\Phi_p$ has a dip lasting months corresponding to the dip observed in the fluxes in (a).

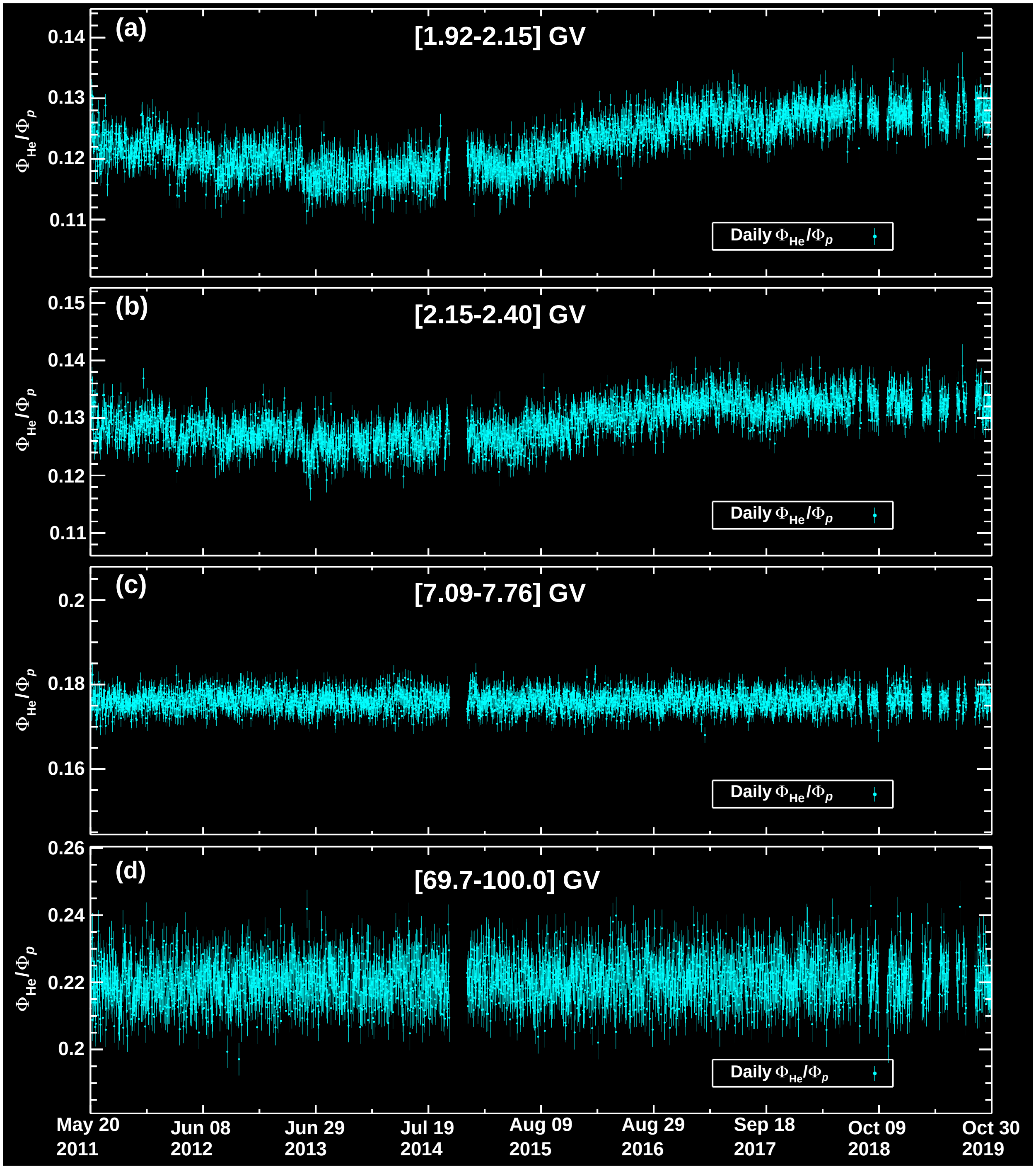

FIG. S21. Daily $\Phi_{\mathrm{He}}/\Phi_p$ measured from May 20, 2011 to October 29, 2019 at (a) [1.92 – 2.15] GV, (b) [2.15 – 2.40] GV, (c) [7.09 – 7.76] GV, and (d) [69.7 – 100.0] GV. As seen, $\Phi_{\mathrm{He}}/\Phi_p$ is time-independent above ~ 7 GV.

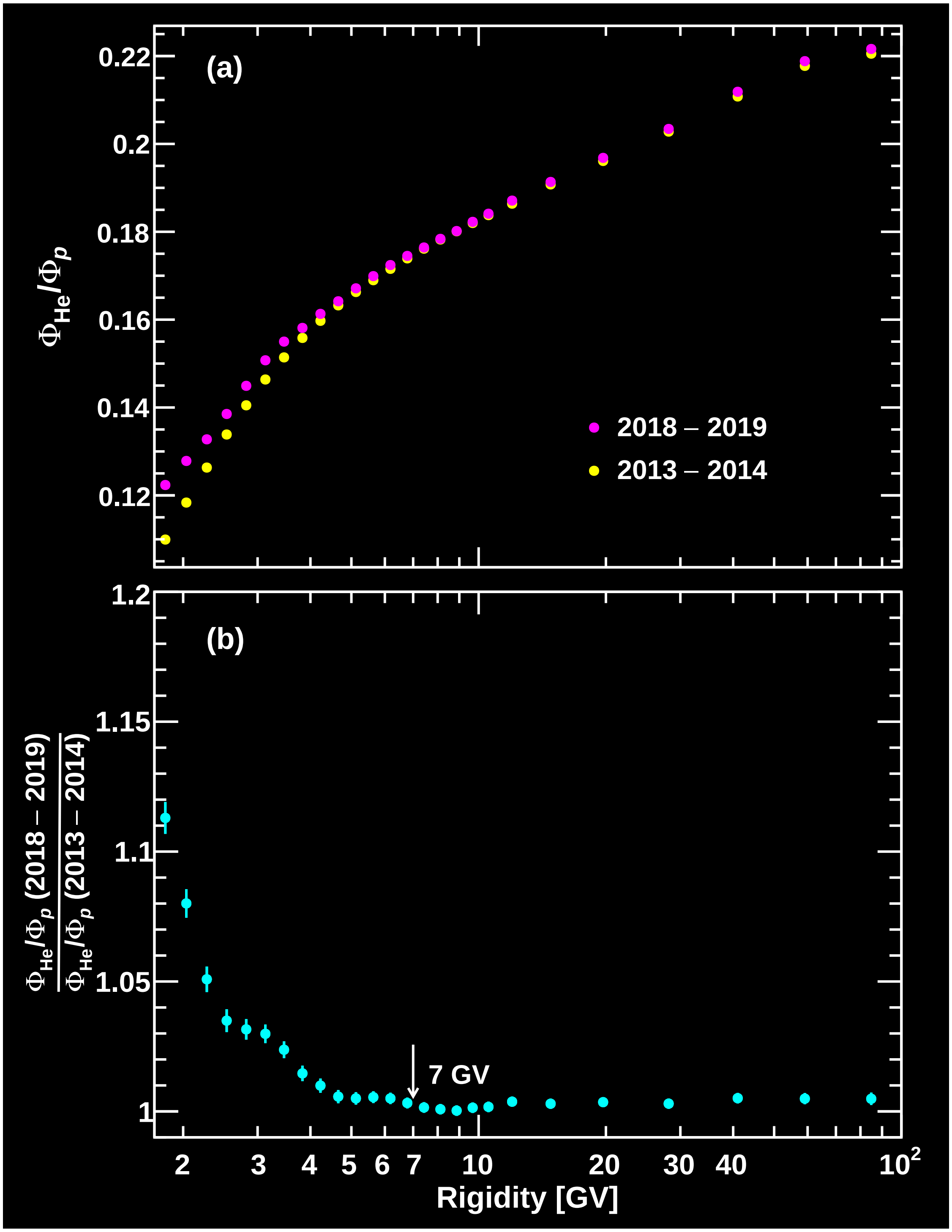

FIG. S22. (a) The comparison of $\Phi_{\mathrm{He}}/\Phi_p$ averaged from 2018 to 2019 (magenta) and from 2013 to 2014 (yellow) as a function of rigidity. (b) The ratio of $\Phi_{\mathrm{He}}/\Phi_p(2018-2019)$ and $\Phi_{\mathrm{He}}/\Phi_p(2013-2014)$ as a function of rigidity. As seen, below ~ 7 GV Φ_{He} exhibits larger time variations than Φ_p.

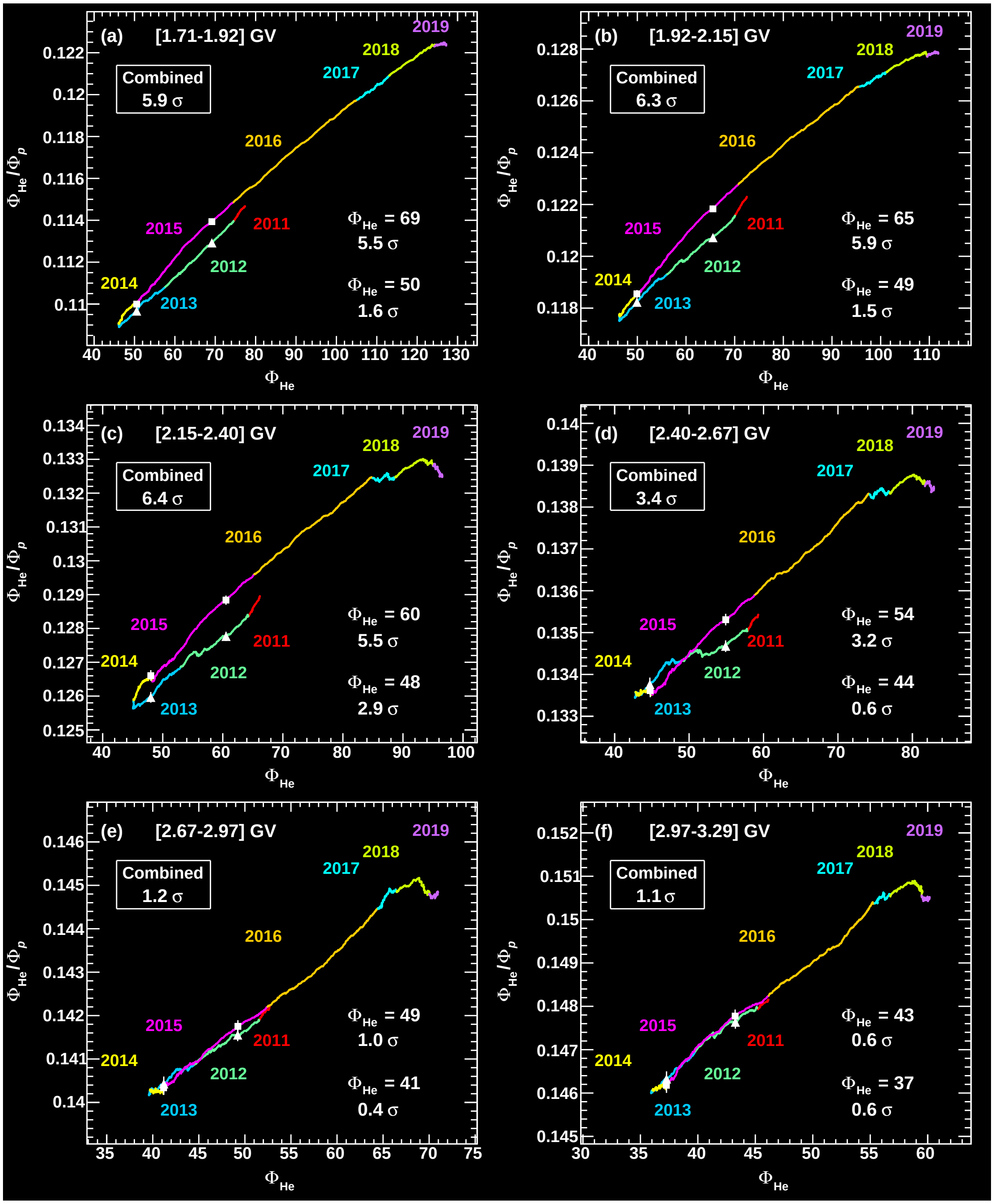

FIG. S23. $\Phi_{\rm He}/\Phi_p$ as a function of $\Phi_{\rm He}$ in units of $[\rm m^{-2}\cdot s^{-1}\cdot sr^{-1}\cdot GV^{-1}]$ for the rigidity bins (a) [1.71 – 1.92] GV, (b) [1.92 – 2.15] GV, (c) [2.15 – 2.40] GV, (d) [2.40 – 2.67] GV, (e) [2.67 – 2.97] GV, and (f) [2.97 – 3.29] GV, both calculated with a moving average of length 14BRs with a step of one day. Different colors indicate different years from 2011 to 2019. The measured $\Phi_{\rm He}/\Phi_p$ together with errors for two pairs of time intervals of 14BRs with the same $\Phi_{\rm He}$ before (white triangles) and after (white squares) the solar maximum in 2014 are shown. The significances (in units of σ) of the difference of $\Phi_{\rm He}/\Phi_p$ with the same $\Phi_{\rm He}$ for the two pairs of time intervals are given. The total significance by combining the significances at two $\Phi_{\rm He}$ values is also given. As seen, the hysteresis is observed at $\sim 6\sigma$ in each of the three consecutive rigidity bins below 2.4 GV, with a combined significance greater than 7σ.

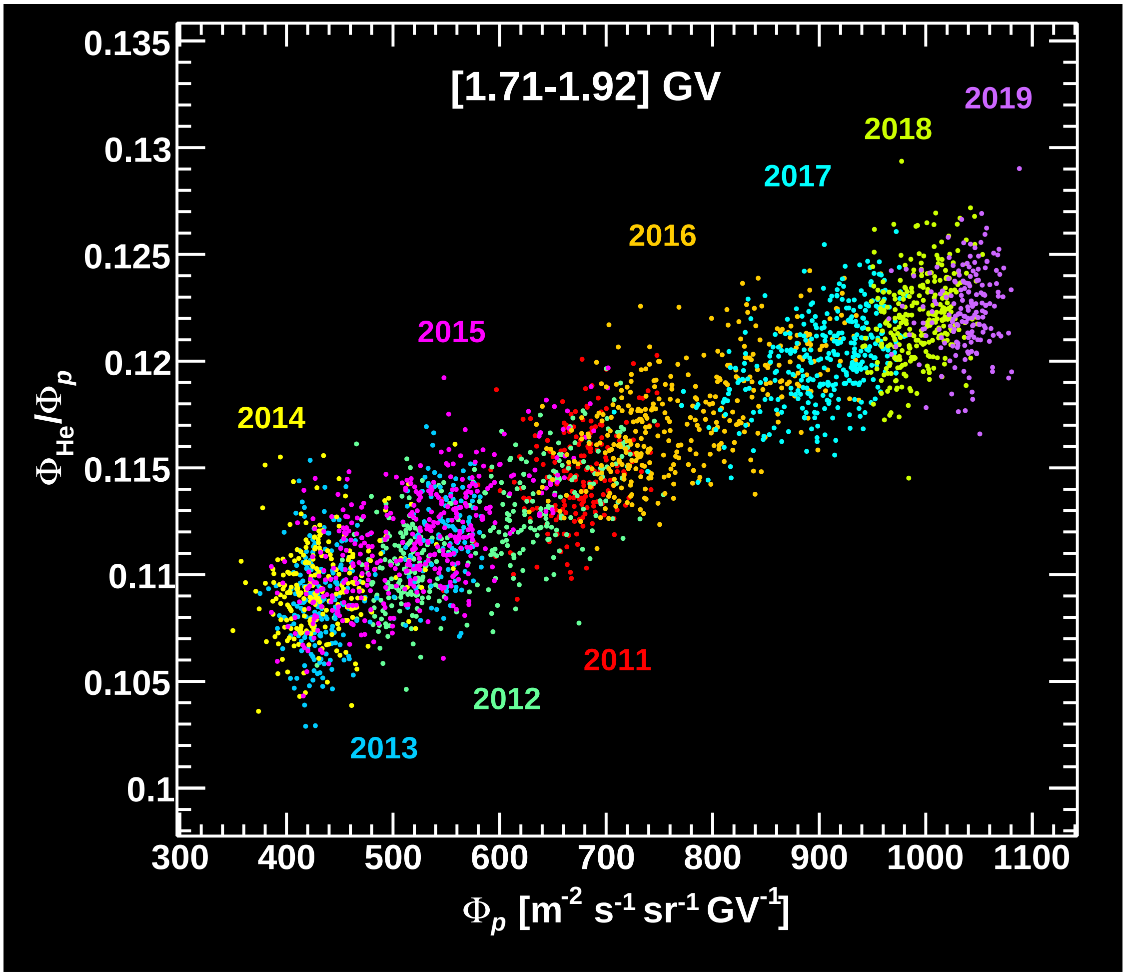

FIG. S24. Daily $\Phi_{\mathrm{He}}/\Phi_p$ as a function of daily Φ_p for the rigidity bin [1.71 – 1.92] GV. Different colors indicate different years from 2011 to 2019.

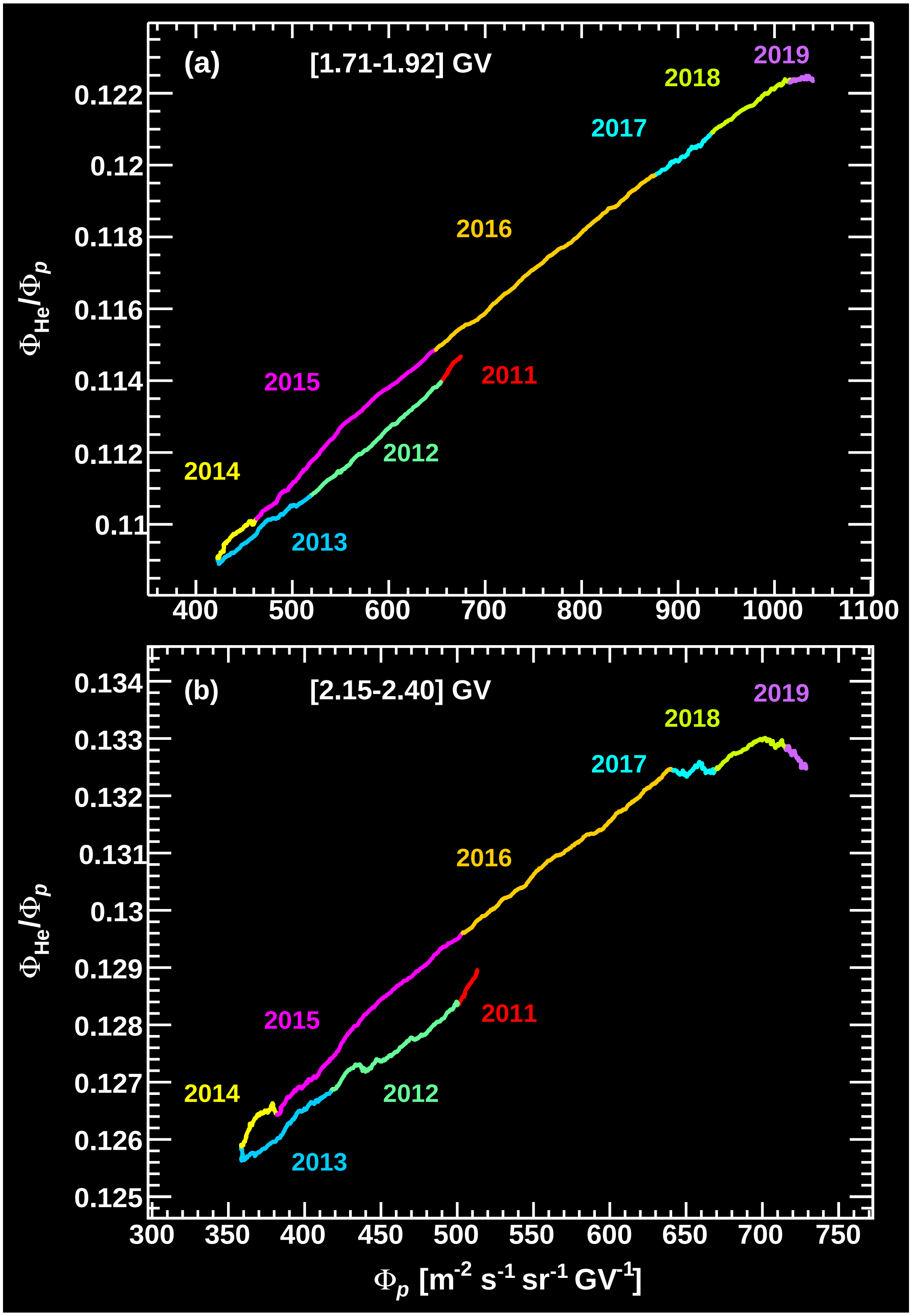

FIG. S25. $\Phi_{\mathrm{He}}/\Phi_p$ as a function of Φ_p both calculated with a moving average of length 14BRs with a step of one day for the rigidity bins (a) [1.71 – 1.92] GV and (b) [2.15 – 2.40] GV. Different colors indicate different years from 2011 to 2019. As seen, below 2.4 GV a hysteresis between $\Phi_{\mathrm{He}}/\Phi_p$ and Φ_p is observed before and after the solar maximum in 2014.

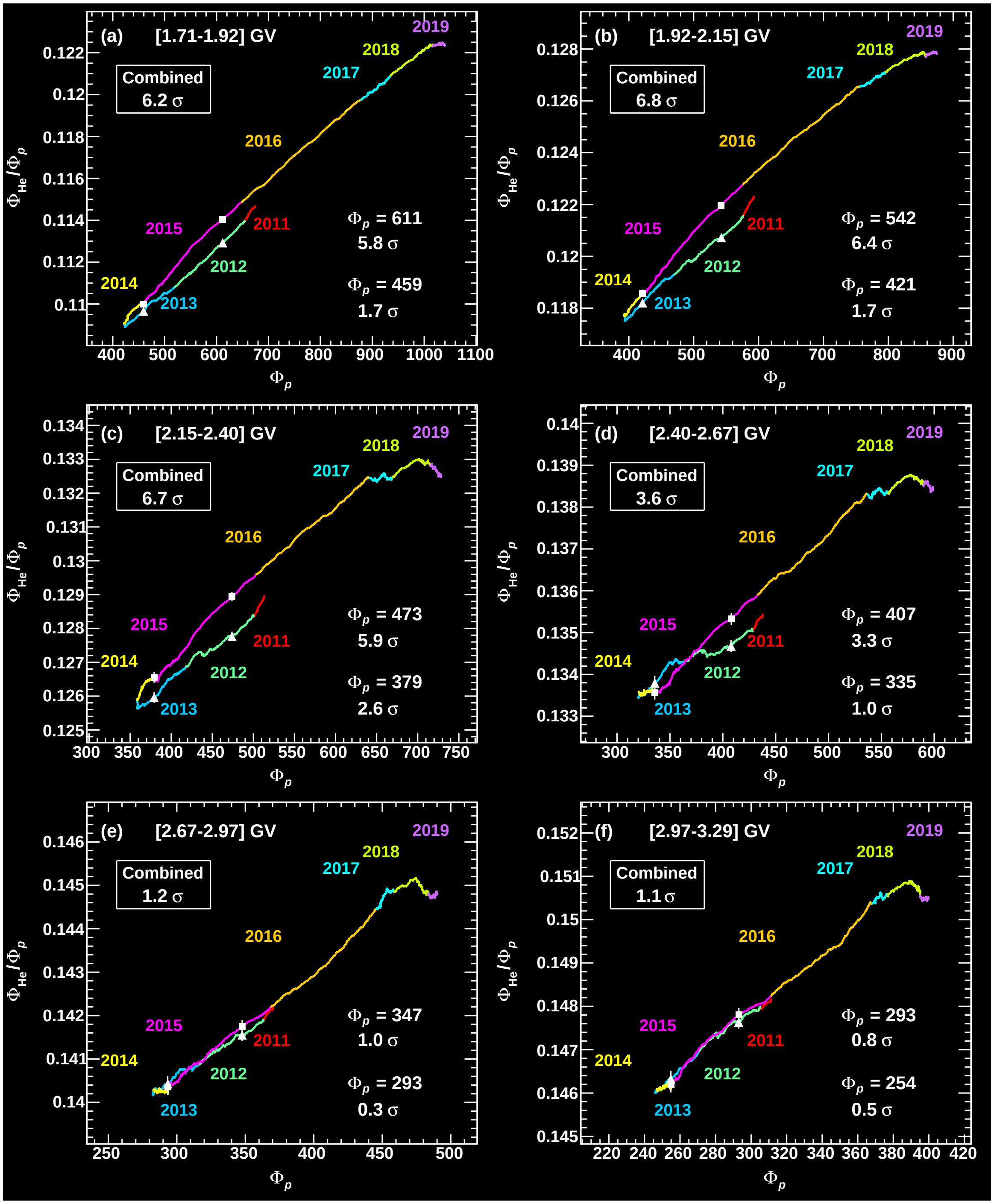

FIG. S26. $\Phi_{\mathrm{He}}/\Phi_p$ as a function of Φ_p in units of $[\mathrm{m}^{-2}\cdot\mathrm{s}^{-1}\cdot\mathrm{sr}^{-1}\cdot\mathrm{GV}^{-1}]$ for the rigidity bins (a) [1.71 – 1.92] GV, (b) [1.92 – 2.15] GV, (c) [2.15 – 2.40] GV, (d) [2.40 – 2.67] GV, (e) [2.67 – 2.97] GV, and (f) [2.97 – 3.29] GV, both calculated with a moving average of length 14BRs with a step of one day. Different colors indicate different years from 2011 to 2019. The measured $\Phi_{\mathrm{He}}/\Phi_p$ together with errors for two pairs of time intervals of 14BRs with the same Φ_p before (white triangles) and after (white squares) the solar maximum in 2014 are shown. The significances (in units of σ) of the difference of $\Phi_{\mathrm{He}}/\Phi_p$ with the same Φ_p for the two pairs of time intervals are given. The total significance by combining the significances at two Φ_p values is also given. As seen, the hysteresis is observed at greater than 6σ in each of the three consecutive rigidity bins below 2.4 GV, with a combined significance greater than 7σ.